INSTITUTE OF PHYSICS PUBLISHING MEASUREMENT SCIENCE AND TECHNOLOGY
Meas. Sci. Technol. **16** (2005) R17–R36 doi:10.1088/0957-0233/16/4/R01

REVIEW ARTICLE

In vivo magnetic resonance imaging: insights into structure and function of the central nervous system

Oliver Natt and Jens Frahm

Biomedizinische NMR Forschungs GmbH am Max-Planck-Institut für biophysikalische Chemie, Am Faßberg 11, 37070 Göttingen, Germany

E-mail: jfrahm@gwdg.de

Received 25 February 2004, in final form 22 November 2004
Published 24 February 2005
Online at stacks.iop.org/MST/16/R17

Abstract
Spatially resolved nuclear magnetic resonance (NMR) techniques provide structural, metabolic and functional insights into the central nervous system and allow for repetitive *in vivo* studies of both humans and animals. Complementing its prominent role in diagnostic imaging, magnetic resonance imaging (MRI) has evolved into an indispensable research tool in system-oriented neurobiology where contributions to functional genomics and translational medicine bridge the gap from molecular biology to animal models and clinical applications. This review presents an overview on some of the most relevant advances in MRI. An introduction covering the basic principles is followed by a discussion of technological improvements in instrumentation and imaging sequences including recent developments in parallel acquisition techniques. Because MRI is noninvasive in contrast to most other imaging modalities, examples focus on *in vivo* studies of the central nervous system in a variety of species ranging from humans to mice and insects.

Keywords: blood oxygenation level dependent (BOLD) contrast, central nervous system (CNS), diffusion, echo-planar imaging (EPI), fast low angle shot (FLASH), magnetic resonance angiography (MRA), magnetic resonance imaging (MRI), magnetization transfer (MT) contrast, nuclear magnetic resonance (NMR), partially parallel acquisition (PPA)

(Some figures in this article are in colour only in the electronic version)

1. Introduction: from NMR to MRI

Almost three decades after the first observations of nuclear magnetic resonance (NMR) in condensed matter by the groups of Felix Bloch and Edmund Purcell, in a seminal work in 1973 [1] Paul Lauterbur described the spatial encoding of NMR signals and its use for imaging, which is the reconstruction of a cross-sectional image from the NMR signals of a three-dimensional object. In 2003 he was awarded the Nobel Prize in Medicine or Physiology together with Peter Mansfield who also made important contributions to the process of image acquisition. The revolutionary invention that led from NMR to magnetic resonance imaging (MRI) has been followed by many more exciting achievements that render MRI not only the method-of-choice for diagnostic imaging but also an important research tool for noninvasive studies of both humans and animals. This particularly applies to investigations that aim at a better understanding of the structure and function of the intact central nervous system (CNS). Thus, 30 years after Lauterbur's invention, state-of-the-art MRI offers an exceptionally broad

spectrum of research opportunities ranging, for example, from basic neurobiology in transgenic mice to functional brain mapping of psychiatric patients.

1.1. Physical principles of NMR

This section reviews the physical principles of NMR insofar as they are necessary to understand the spin manipulations used in MRI. The theoretical description closely follows the article by Dixon and Akstrand [2]. It focuses on proton NMR, because the proton is the most frequently used nucleus for MRI due to its high gyromagnetic ratio, natural abundance and concentration in biologic tissue in the form of water and fat.

By virtue of its spin angular momentum $\boldsymbol{I}$ the proton possesses a magnetic dipole moment $\boldsymbol{\mu} = \gamma \boldsymbol{I}$ with $\gamma = 2\pi \times 42.58$ MHz T^{-1} the proton gyromagnetic ratio. In an external magnetic field $\boldsymbol{B}_0 = B_0 \boldsymbol{e}_z$ the proton is in one of two energy states which are separated by $\Delta E = \gamma \hbar B_0$ (Zeeman effect). In thermal equilibrium, the number of protons in the lower energy state is slightly larger than the number in the high energy state. This population difference results in a net magnetization [3]

$$\boldsymbol{M} = \rho \langle \boldsymbol{\mu} \rangle = \rho \frac{\gamma^2 \hbar^2 j(j+1)}{3kT} B_0 \boldsymbol{e}_z \tag{1}$$

with ρ the proton density in the sample, $j = 1/2$ the spin quantum number of the proton, T the temperature and k Boltzmann's constant. Because the magnetic moment $\boldsymbol{\mu}$ is proportional to the spin $\boldsymbol{I}$, the commutation relations for the spin can be used to calculate the equation of motion for the magnetization

$$\frac{\mathrm{d}}{\mathrm{d}t}\boldsymbol{M} = \gamma \boldsymbol{M} \times \boldsymbol{B}. \tag{2}$$

Except for a collinear orientation of the magnetization $\boldsymbol{M}$ and the external magnetic field $\boldsymbol{B}$, this equation yields a precession of the magnetization vector with the angular frequency $\omega = \gamma B$. For an NMR experiment the total magnetic field $\boldsymbol{B} = \boldsymbol{B}_0 + \boldsymbol{B}_1$ includes the static magnetic field $\boldsymbol{B}_0$ (oriented along the z-direction) and the radiofrequency (RF) field $\boldsymbol{B}_1$ (applied in a perpendicular orientation). Accordingly, in a frame rotating with the angular velocity $\omega_0 = \gamma B_0$, the effect of the static magnetic field is eliminated, and equation (2) reads

$$\frac{\mathrm{d}}{\mathrm{d}t}\boldsymbol{M} = \gamma \boldsymbol{M} \times \boldsymbol{B}_1. \tag{3}$$

Because this classic description neglects molecular interactions between different protons, Bloch added phenomenological relaxation terms according to [4]

$$\frac{\mathrm{d}}{\mathrm{d}t}\boldsymbol{M} = \gamma \boldsymbol{M} \times \boldsymbol{B}_1 + \boldsymbol{R}\boldsymbol{M} + \begin{pmatrix} 0 \\ 0 \\ 1/T_1 \end{pmatrix} M_0 \tag{4}$$

with

$$\boldsymbol{R} = \begin{pmatrix} -1/T_2 & 0 & 0 \\ 0 & -1/T_2 & 0 \\ 0 & 0 & -1/T_1 \end{pmatrix}. \tag{5}$$

The Bloch equations (4) and (5) have several consequences. First of all, a short RF pulse $\boldsymbol{B}_1(t)$ tilts the magnetization vector $\boldsymbol{M}$ by an angle—the so-called flip angle—which is proportional to the integral of the RF pulse. Secondly, after RF excitation, the precession of the magnetization vector with the Larmor frequency $\omega_0 = \gamma B_0$ produces an oscillating magnetic field which is perpendicular to $\boldsymbol{B}_0$. The concomitant induction of a current in a receive coil is acquired and analysed in an NMR experiment. The signal which directly follows an excitation pulse is called free induction decay (FID). And thirdly, the excited transverse magnetization, which is the component of $\boldsymbol{M}$ in the x–y-plane, exponentially decays with the spin–spin relaxation time T_2, and the longitudinal magnetization, which is the z-component of $\boldsymbol{M}$, returns to its equilibrium value M_0 with the spin-lattice relaxation time T_1.

1.2. Signal localization

Lauterbur proposed the use of gradient fields to localize the NMR signal [1]. A gradient field is an idealized magnetic field the magnitude of which depends on the position according to

$$\boldsymbol{B}(\boldsymbol{r}) = \begin{pmatrix} 0 \\ 0 \\ \boldsymbol{G}\boldsymbol{r} \end{pmatrix}. \tag{6}$$

Thus, as long as the excited transverse magnetization in an NMR experiment precesses in the presence of such a gradient field, its Larmor frequency depends on the position according to

$$\Delta\omega(\boldsymbol{r}) = \gamma \boldsymbol{G}\boldsymbol{r}. \tag{7}$$

If a gradient field is applied during data acquisition, then the Fourier transform (FT) of the time-domain data yields a frequency spectrum which represents a one-dimensional intensity projection of the sample along the gradient direction. This spatial encoding of the NMR frequency can be performed with any of the three basic NMR or MRI signals depicted in figure 1: a gradient echo which is generated by a single RF pulse and two consecutive gradient pulses of opposite sign, a spin echo which refocuses the initial FID by a combination of two RF pulses (usually 90° and 180° pulses) in the presence of a pair of compensating gradients, and a stimulated echo which requires three successive RF pulses (usually 90° pulses) for refocusing [5].

1.3. Image acquisition and reconstruction

In order to facilitate the understanding of image acquisition and reconstruction in MRI, the concept of k-space has been shown to be highly advantageous. The signal S measured in an MRI experiment is the integral of the complex transverse magnetization $M_\perp = M_x + \mathrm{i}M_y$ of the sample. Using the Bloch equation (4) the transverse magnetization at a position $\boldsymbol{r}$ is given by the FT of the measured signal $S(\boldsymbol{k})$

$$M_\perp(\boldsymbol{r}) = \int S(\boldsymbol{k}) \exp(-\mathrm{i}\boldsymbol{k}\boldsymbol{r})\, \mathrm{d}^3k \tag{8}$$

where $\boldsymbol{k}(t)$ denotes the time integral of the gradient fields after excitation

$$\boldsymbol{k} = \gamma \int_0^t \boldsymbol{G}(\tau)\, \mathrm{d}\tau. \tag{9}$$

Using the k-space formalism, the MRI acquisition can be understood as a discrete sampling of its Fourier transform.

Figure 2 shows a generic fast low angle shot (FLASH) MRI sequence as the prototype of rapid gradient-echo imaging

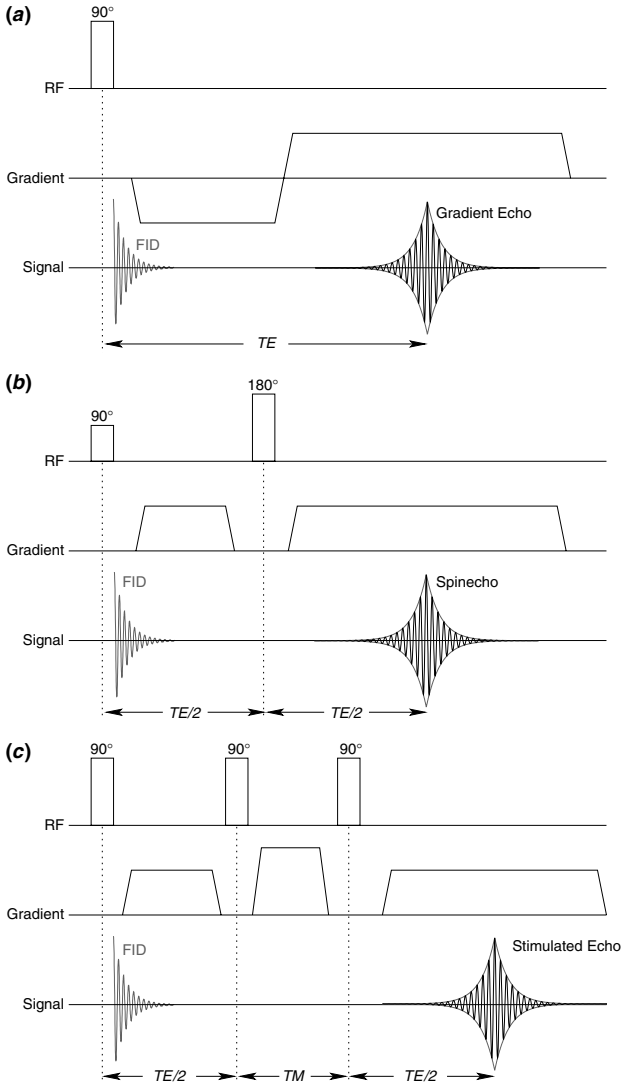

Figure 1. Schematic diagrams for the acquisition of frequency-encoded NMR signals using (*a*) a gradient echo, (*b*) a spin echo and (*c*) a stimulated echo. TE refers to the echo time. The time between the second and third RF pulses in a stimulated echo sequence is called the mixing time TM.

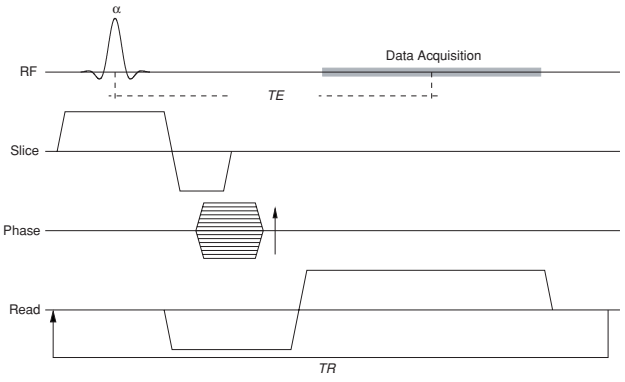

Figure 2. Schematic diagram of a gradient-echo MRI sequence (FLASH) employing slice selection, phase encoding and frequency encoding.

techniques [6]. RF excitation in the presence of a gradient restricts the frequency-selective excitation (as given by the characteristics of the pulse shape) to a section perpendicular to the gradient direction. In one of the remaining dimensions, a phase-encoding gradient with variable amplitude precedes the application of a frequency-encoding gradient in the third dimension. This sequence of events acquires only a single gradient echo (or line in *k*-space)—it needs to be repeated to fully cover the phase-encoding dimension of the image. The corresponding sampling of *k*-space along a rectangular grid is shown in figure 3(*a*). The real part of the acquired data matrix is depicted in figure 3(*b*), while figure 3(*c*) demonstrates the resulting image obtained after two-dimensional (2D) FT of the *k*-space data.

The imaging scheme described above is normally referred to as 2D MRI. Alternatively, 3D MRI sequences require the application of a second independent phase-encoding gradient in the slice-selection direction followed by 3D FT for image reconstruction. Rapid 3D MRI acquisitions based on the FLASH principle [7] are a preferred option for high-resolution MRI at isotropic spatial resolution.

In order to overcome the limitations given by the Nyquist theorem, it has been proposed to restrict the excited magnetization in two rather than only one direction by the application of two-dimensional spatially-selective RF (2DRF) pulses. Although multidimensional spatially-selective RF excitations were theoretically described and experimentally realized more than a decade ago [8], their practical implementation has only recently been facilitated by considerable advances in gradient hardware initiated by the increasing demand for high-speed MRI (see [9] and references cited therein).

A different approach to reduce the number of phase-encoding steps in MRI is known as partial Fourier phase encoding. It depends on the complex conjugate symmetry of *k*-space and omits the acquisition of, for example, half of the *k*-space except for a few central lines. Partial Fourier imaging has been successfully applied to single-shot acquisition techniques such as fast spin-echo MRI [10, 11], echo-planar imaging [12] and single-shot STEAM MRI [13]. An extensive discussion of the possible reconstruction algorithms for partial Fourier data can be found in [14].

2. Instrumentation

The first 20 years of MRI development were dominated by a steady increase of the commercially available 'clinical' field strength from about 0.1 T to 1.5 T or even 3 T. More recently, however, a major technological breakthrough has been achieved which is expected to further revolutionize MRI within the foreseeable future. Pertinent approaches rely on the extensive use of multiple receiver coils which gain either SNR per measuring time or, perhaps even more importantly, imaging speed via parallel acquisition techniques.

Figure 4 shows a modern 3 T MRI system as offered by major manufacturers. Such systems emerge as a *de facto* industry standard—at least for high-performance studies of the human brain. In fact, some researchers still attempt to explore the potential of 7 T or 9.4 T whole-body MRI systems, although the utility and benefits of ultra-high field strengths, both in the field of small animal MRI and human MRI, remain

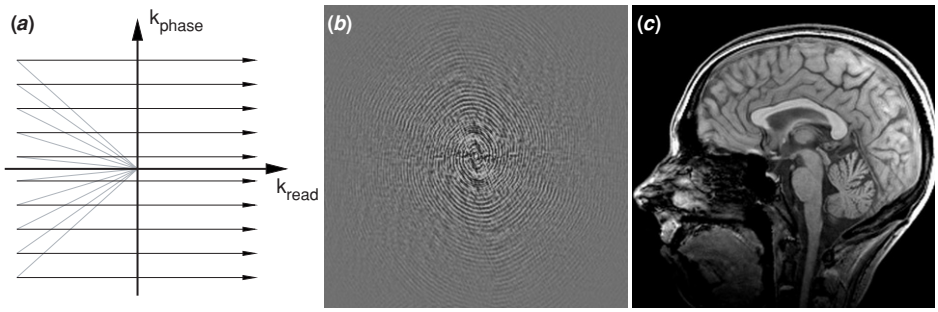

Figure 3. (*a*) Sampling of *k*-space for Fourier imaging. The grey lines indicate the effect of the phase-encoding gradient and the dephasing part of the frequency-encoding 'readout' gradient. Black lines correspond to the application of the actual readout gradient. (*b*) Acquired *k*-space data and (*c*) corresponding image reconstructed by two-dimensional FT.

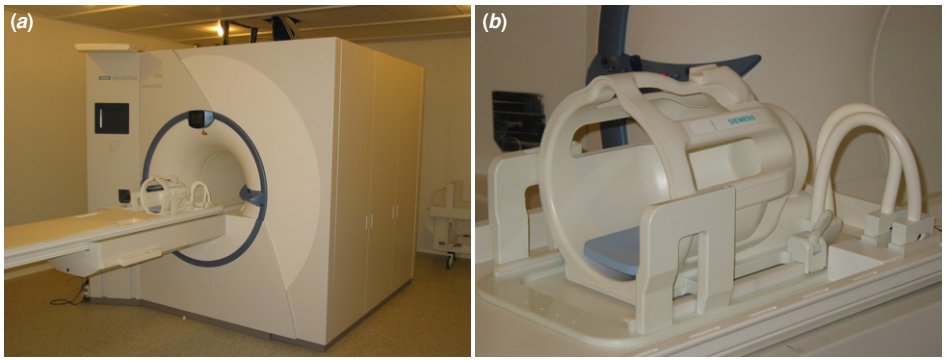

Figure 4. (*a*) Whole-body 3 T MRI system (Magnetom Trio, Siemens, Erlangen, Germany) and (*b*) 8-channel phased-array head coil.

unclear. This is because the promises of improved SNR—at least for proton MRI—are counterbalanced by several undesired factors. Respective problems that increase with field strength include difficulties in achieving a homogeneous RF excitation (due to disturbing effects from dielectric resonances and electric conductivity problems), increased absolute magnetic field inhomogeneities and susceptibility artefacts (causing geometric image distortions and focal signal void), increased physiological noise and motion sensitivity (lowering the theoretically expected gain in SNR and affecting the image quality in functional brain mapping), quadratically increased RF power deposition (reducing volume coverage, that is the number of simultaneously acquired sections, or reducing the speed of data acquisition), and vestibular stimulation (causing nausea while moving inside the magnet). Moreover, with a few exceptions such as improved background signal suppression in angiographic MRI, the increased ratio of the relaxation times T_1/T_2 with field strength has a negative impact on most MRI sequences [15, 16]. For example, in mouse brain a T_1/T_2 ratio of 9 at 1.5 T has been reported to increase to 60.5 at 11.5 T [17].

Parallel to the development of stronger magnets there has been a continuous improvement of the gradient systems required for spatial encoding. For human MRI, sufficiently linear gradients with a strength of 40 mT m^{-1} and slew rates of 200 mT m^{-1} ms^{-1} are now commonly in use. The availability of gradient systems which are not only strong and fast but also generate fewer eddy currents even allows for the realization of sensitive high-speed MRI sequences such as true FISP which—in a slower mode—are prone to artefacts from resonance offset effects (see below).

As mentioned above, an extremely important factor for the overall quality of an MRI study is the proper design of a suitable RF coil or array of coils. Phased array coils were first proposed in order to combine the high sensitivity of a small surface coil with the more extended field-of-view (FOV) covered by a larger volume coil [18]. However, the use of phased array coils has been dramatically expanded with the advent of parallel acquisition techniques (see section 3.2). In order to take advantage of pertinent approaches, MRI systems need to be equipped with a large number of independent RF receiver channels. Currently, systems with up to 64 channels are already available, while applications to the human brain employ coils with 8 to 12 elements.

3. MRI sequences

Apart from improvements in the system hardware, the development of novel RF pulse and gradient sequences perpetually opened new applications for MRI. Research in MRI sequence design has two major focuses—acquisition speed and access to new (specific) contrasts. For an introduction to rapid scan MRI, see [19].

3.1. Fast imaging techniques

In 1985 the development of a rapid imaging sequence based on gradient-echo signals reduced the acquisition times of 2D or 3D images by about two orders of magnitude. In fact, FLASH MRI is nowadays one of the workhorses for clinical MRI. The enormous gain in speed not only improved patient comfort, but

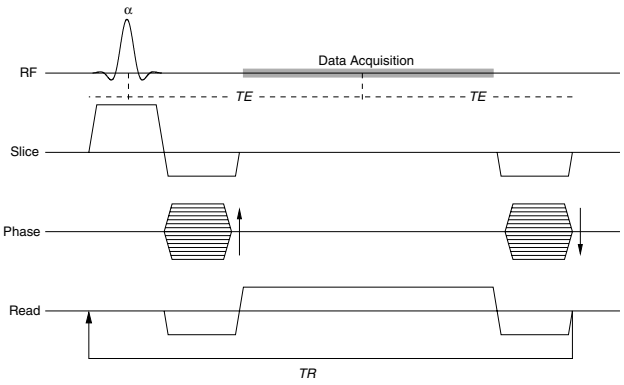

Figure 5. Schematic diagram for true FISP MRI. The fully balanced sequence generates an overlap of the gradient echoes from the SSFP-FID and SSFP-echo.

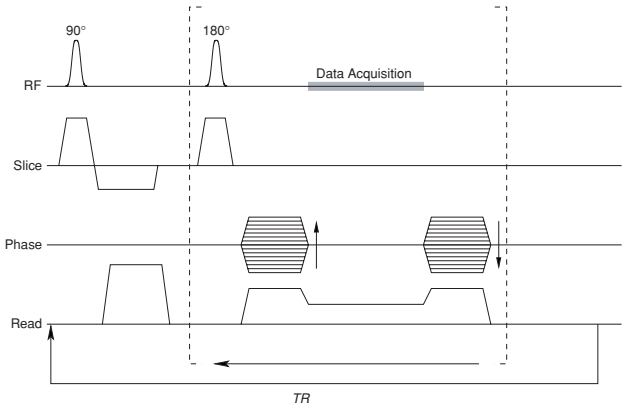

Figure 6. Schematic diagram for fast spin-echo MRI (FSE). The sequence covers multiple *k*-space lines per RF excitation using different phase encodings for the echoes of a multi-echo train. The phase encoding must be rephased in each echo interval.

also allowed for imaging within a single breath-hold, ECG-synchronized 'filming' of the heart, or a delineation of complex anatomies using 3D MRI at isotropic spatial resolution.

The principle of the FLASH sequence [6] as sketched in figure 2 is to excite the sample with a small flip angle pulse (e.g., $\alpha = 5$–25°), acquire a gradient-recalled echo, and repeat this process with a repetition time much shorter than the T_1 relaxation time (e.g., TR = 5–15 ms). During imaging the resulting dynamic equilibrium magnetization yields a steady-state free precession (SSFP) signal that in the presence of suitable frequency-encoding imaging gradients may be acquired as a gradient echo of either the SSFP-FID or the SSFP-echo signal [20] or both [19, 21]. In order to achieve spin-density or T_1-weighted images, the FLASH sequence uses the SSFP-FID signal in conjunction with an efficient dephasing ('spoiling') of incorrectly phase-encoded SSFP signals by post-acquisition spoiler gradients or phase-cycled RF excitations [22]. Current implementations of spoiled FLASH use both mechanisms in combination with a reversed phase-encoding gradient ('rewinder') after the end of data acquisition.

A fully refocused and balanced version of SSFP imaging termed true FISP [21] (fast imaging with steady-state precession) is shown in figure 5. The sequence coherently adds the gradient echoes of the SSFP-FID and SSFP-echo signal with the advantage of providing the highest possible SNR per measurement time of all steady-state sequences. Although true FISP applications to brain and spine were proposed years ago [21, 23], only recent improvements in gradient hardware have allowed for sufficiently short repetition times of the order of a few milliseconds. This speed is necessary to ameliorate the sensitivity of the balanced SSFP signal to magnetic field inhomogeneities (resonance offset effects) which otherwise lead to interference stripes in the images. Because true FISP combines high speed with good contrast between blood and myocardium due to respective differences in the T_1/T_2 ratio, the main focus of true FISP is in the field of cardiac MRI [24]. In the brain, true FISP is especially used for imaging of the internal auditory canals.

While rapid low-flip angle gradient-echo sequences speed up MRI by a shortening of the repetition time, fast spin-echo (FSE) sequences acquire more than one *k*-space line per RF excitation (or even all after a single excitation). As originally proposed by Hennig *et al* in 1984 [25, 26] and shown in figure 6, the rapid acquisition with relaxation enhancement (RARE) technique takes advantage of a Carr–Purcell–Meiboom–Gill (CPMG) echo train [27, 28] in which the individual echoes are differently phase encoded (e.g., 8–16 echoes for FSE or up to 128 echoes for RARE). The primary aim of FSE MRI sequences is to provide T_2 contrast, while spin-density contrast is attainable for short (mean) echo times in conjunction with long repetition times. On high-field MRI systems the use of FSE sequences is limited by the RF power deposition which quadratically increases with frequency (or field strength). This problem particularly affects FSE MRI because of the large number of 180° refocusing pulses. To comply with RF safety regulations, it is common practice to reduce the flip angle of the refocusing pulses from 180° to, for example, 120° with only a minor impact on SNR and contrast [29]. Further alternatives are the incorporation of additional gradient echo signals accompanying each spin echo [30] or the use of the hyperecho concept [31] which exploits the properties of the SSFP signal by a specific modulation of the flip angles and phases of the refocusing RF pulses.

The generic MRI sequence for single-shot imaging with acquisition times of less than 100 ms was proposed as early as 1977 by Mansfield and termed echo-planar imaging (EPI) [32, 33]. In modern implementations the sequence generates a multi-echo gradient-echo train by multiple reversals of the frequency-encoding gradient. The echoes are differently phase-encoded by brief cumulative phase-encoding gradient pulses ('blips') which are applied in between successive echoes. The corresponding sequence diagram and *k*-space trajectory are shown in figure 7. To symmetrically cover *k*-space, the phase-encoding blips are preceded by a dephasing gradient pulse which moves the start of the trajectory to the outer boundary of *k*-space. This choice simplifies the image reconstruction as it mimics conventional spin-warp Fourier imaging and therefore does not require data interpolation to a rectangular grid before 2D FT [34].

The high speed of EPI is partly at the expense of image quality [35]. First of all, the gradient-echo signals decrease with the effective spin–spin relaxation time $T_2^\star$, so that the long train of echoes leads to a pronounced sensitivity to magnetic field inhomogeneities and tissue

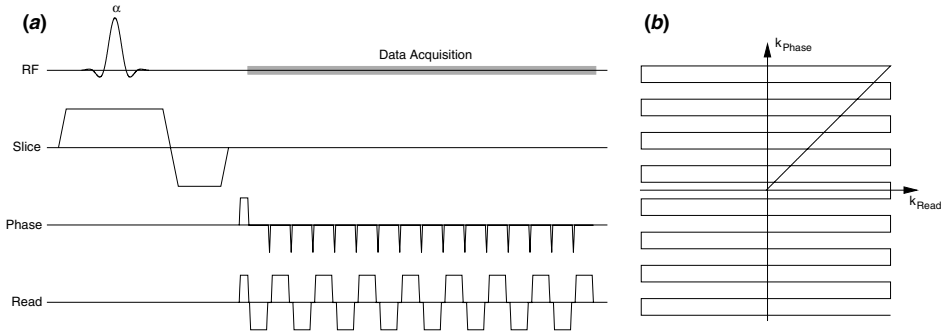

Figure 7. (*a*) Schematic diagram and (*b*) *k*-space trajectory for single-shot gradient-echo EPI.

susceptibility differences. Apart from geometric distortions and focal signal void, the echo decay along the phase-encoding direction causes ringing artefacts and image blurring due to the truncation of high spatial frequencies for short $T_2^\star$ components. A second prominent artefact originates from the fact that neighbouring lines in *k*-space are scanned with opposite direction, that is EPI uses odd and even echoes with either positive or negative frequency-encoding gradients. Small but unavoidable differences, for example due to eddy currents, cause periodic signal fluctuations that translate into a ghost image along the phase-encoding dimension of the reconstructed image. Although such odd–even discontinuities are commonly treated by a post-acquisition phase correction using data from pre-recorded gradient echoes without phase-encoding, the resulting images frequently suffer from residual ghosting. A third class of artefacts stems from off-resonance effects. They represent signal contributions with different chemical shifts such as fat or susceptibility-shifted water resonances that vary between in-phase and opposed-phase conditions in sequential gradient echoes. The presence of fat signals is typically addressed by chemical-shift selective (CHESS) [36] or binomial frequency-selective RF pulses which saturate respective protons immediately before the actual EPI acquisition.

As far as applications are concerned, the natural target of a high-speed MRI sequence would be cardiac imaging. Although early EPI studies indeed addressed snapshot imaging of the heart [37, 38], not much work has followed. This may be explained by a better recognition of the detrimental effects on image quality from some of the aforementioned problems. More recent EPI studies have focused on the brain where the main applications are functional MRI and diffusion-weighted MRI. Such techniques are discussed in detail in sections 5.1 and 5.2, respectively.

As an alternative to EPI, an efficient single-shot traversal of *k*-space may be accomplished by spiral trajectories, which require the combination of two sinusoidally oscillating gradients of increasing amplitude [39]. Figure 8 depicts a spiral MRI sequence with coverage of *k*-space by a round spiral (other forms are also possible). Rather than emphasizing the single-shot capabilities, practical implementations often rely on interleaved multi-shot applications, that is segmented scanning, in order to alleviate some of the image blurring which results from $T_2^\star$ problems. In contrast to EPI, the acquired *k*-space data need to be interpolated onto a rectangular grid prior to 2D FT image reconstruction. The calculation of suitable gradient waveforms, the utility of different image reconstruction algorithms and a discussion of related artefacts in spiral imaging have been reviewed by Börnert *et al* [40] and Block [41].

3.2. Parallel acquisition techniques

Further reductions of MRI scanning times beyond the aforementioned advances are hampered by a variety of practical limitations. For multi-shot sequences such as FLASH or SSFP in general, the minimum TR is determined by the gradient performance and the durations needed for slice-selective RF excitation and phase encoding. The use of even stronger and faster gradient switches as currently available is restricted by safety regulations which limit the maximum slew rate in order to avoid peripheral nerve stimulation. On the other hand, for single-shot techniques such as EPI or RARE, the achievable spatial resolution is limited by the $T_2^\star$ or T_2 signal decay along the echo train, respectively. An exciting solution to many of these problems originates from parallel acquisition techniques which promise to speed up the imaging process by another order of magnitude at the expense of some SNR.

The basic principle of parallel acquisition techniques in MRI is to acquire fewer data than necessary for a conventional Fourier image—but simultaneously from multiple independent receive coils. While commercially available setups use 4 to 12 different coils per body part, experimental designs already test the use of 64 elements for a headcoil. The spatially distinct sensitivities of the individual coils provide additional information that allows for a reconstruction of undistorted images even from undersampled data, that is from recordings with a lower number of *k*-space lines or phase-encoded echo signals. Reconstruction techniques for parallel acquisitions can be separated into two categories, that is methods based on *k*-space and image space, respectively.

3.2.1. Parallel acquisition methods based on k-space. In 1997 Sodickson *et al* [42] proposed a method termed simultaneous acquisition of spatial harmonics (SMASH) which is the prototype of a reconstruction technique based on *k*-space information. For a linear array of surface coils as shown in figure 9(*a*) (top) conventional phase encoding is performed for only a subset of *k*-space indicated by solid lines in figure 9(*b*). Missing lines are calculated using both

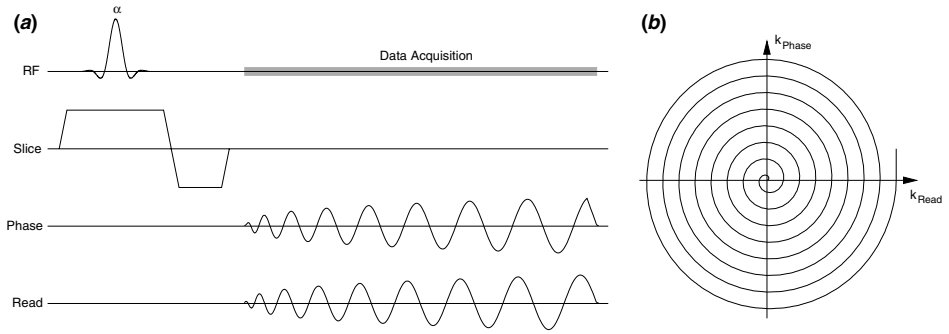

Figure 8. (*a*) Schematic diagram and (*b*) *k*-space trajectory for single-shot gradient-echo spiral MRI.

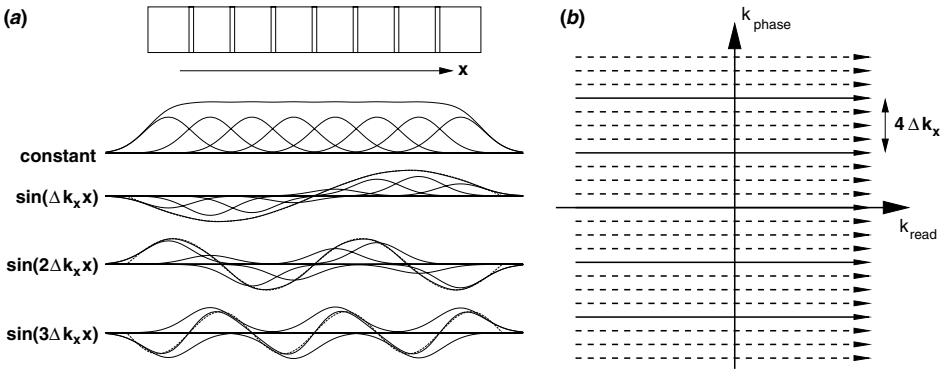

Figure 9. Parallel MRI using the SMASH method (reduction factor 4). (*a*) Using an array of multiple receiver coils, the acquisition of spatial harmonics is accomplished by conventional phase encoding. While thin lines refer to the weighted sensitivity profiles of the individual coil elements, thick lines represent the combined sensitivity profiles which closely approximate spatial harmonics. (*b*) Because only a subset of the k-space lines is directly acquired by phase encoding (solid), missing lines (dashed) are interpolated from the measured lines by the different combinations of the individual coils shown in (*a*).

the weighted sums of the signals from the individual coils and their individual sensitivity profiles. The corresponding overall sensitivity profile is either approximately constant or represents a spatial harmonic as shown in figure 9(*a*) (bottom). The ratio of the total *k*-space lines and the actually sampled *k*-space is referred to as the reduction factor which roughly corresponds to the acceleration factor in terms of image acquisition time.

The quality of image reconstruction depends on the accuracy with which the individual coil sensitivities are known. This problem hampers the practical application of SMASH as many subject-dependent factors affect the coil loading *in vivo*. In order to overcome these limitations, autocalibrating SMASH [43] and variable density SMASH with autocalibration [44] use a small number of additional lines in *k*-space which then help to better define the complex weighting factors for the interpolation of the missing *k*-space lines. Full sampling of the centre of *k*-space is particularly effective in reducing the power of residual aliasing artefacts. Because such techniques rely on only a partial undersampling of *k*-space, they are generally referred to as partially parallel acquisition (PPA) strategies.

A further improvement has been accomplished with the introduction of a technique termed generalized autocalibrating PPA (GRAPPA) [45]. Here, not only the directly adjacent *k*-space lines but also larger blocks of truly phase-encoded lines are used to reconstruct a missing line. The GRAPPA method extends the application of *k*-space PPA reconstructions to coil designs, which do not allow for a perfect fit of spatial harmonics.

3.2.2. Parallel acquisition methods based on image space. In contrast to the PPA reconstruction techniques discussed above, subencoding developed by Ra *et al* [46] in 1993 and sensitivity encoding (SENSE) by Pruessmann [47] in 1999 exploit a more intuitively understandable approach in the image space. The basic principle is illustrated in figure 10. Formal reconstructions of the undersampled *k*-space data from the two simultaneous scans yield aliased images (figures 10(*b*) and (*d*). Provided that the coil sensitivity profiles are known, the aliased images can be unfolded by solving a system of linear equations. While the first subencoding technique [46] was limited to reduction factors equal to the number of coil elements, the SENSE method [47] overcomes this restriction.

3.2.3. Applications. Most modern MRI systems offer multichannel receiver systems, phased-array coils with multiple elements, and parallel acquisition techniques with GRAPPA and/or SENSE for image reconstruction. While both GRAPPA and SENSE are compatible with all Fourier MRI sequences, SENSE is even applicable to non-Cartesian *k*-space trajectories such as spirals [48].

In general, PPA techniques provide an acceleration of the data acquisition at the cost of SNR [47]. Relative to the SNR_{full}

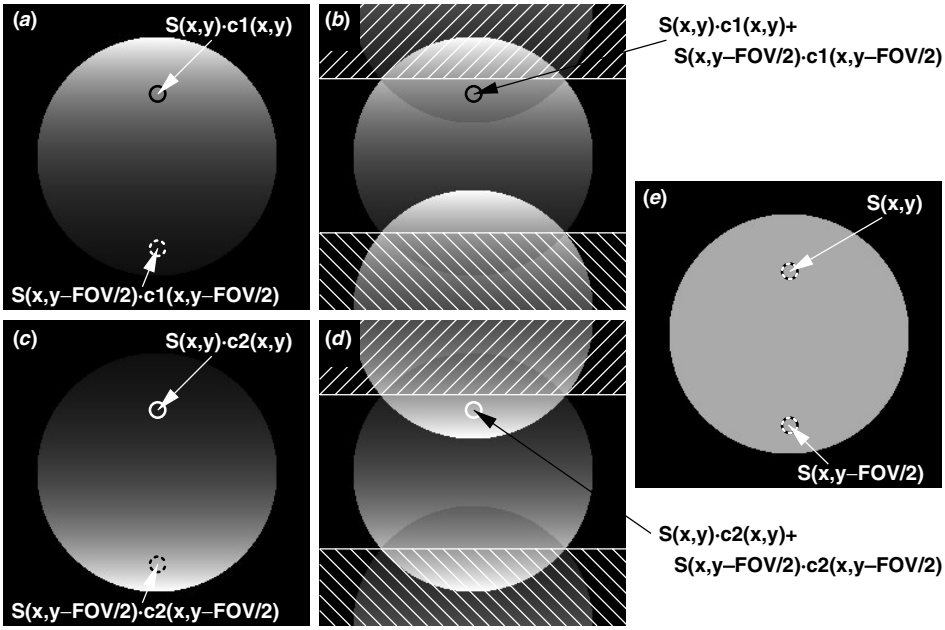

Figure 10. Parallel MRI using the SENSE method (reduction factor 2). (*a*), (*c*) The full Fourier acquisition of two images with two surface coils leads to a multiplication of the theoretically expected signal $S(x, y)$ with the corresponding coil sensitivity profiles $c1(x, y)$ and $c2(x, y)$, respectively (FOV = field-of-view). (*b*), (*d*) The omission of every other line in *k*-space reduces the acquisition time by a factor of 2 but causes aliasing artefacts. (*e*) The original image intensities can be calculated from the aliased images by solving a system of linear equations.

of a full *k*-space acquisition, the $\mathrm{SNR}_{\mathrm{ppa}}$ of a corresponding PPA acquisition yields

$$\mathrm{SNR}_{\mathrm{ppa}} = \frac{\mathrm{SNR}_{\mathrm{full}}}{g\sqrt{R}} \tag{10}$$

with R the reduction factor and $g \geqslant 1$ a geometric factor which strongly depends on the coil. Together with the fact that small coils are more easily adapted to high frequencies, the SNR penalty renders PPA applications especially attractive for MRI at high magnetic fields.

While the improvement in speed is a great benefit on its own, PPA techniques also bear the potential of improving the quality of (single-shot) gradient-echo images. This particularly holds true for EPI, where—for a given spatial resolution—PPA schemes allow for a shortening of the length of the echo train compared to a full *k*-space acquisition. The concomitant reduction of the sensitivity to magnetic field inhomogeneities yields less geometric distortion and signal void as, for example, demonstrated for diffusion-weighted EPI [49, 50].

An interesting application of PPA techniques arises for combinations with single-shot stimulated echo acquisition mode (STEAM) MRI sequences [51]. The sequence replaces the final 90° RF pulse of a basic 90°–90°–90° STEAM MRI sequence [52] by a series of low-flip angle read pulses that successively translate the longitudinal magnetization prepared by the first two 90° RF pulses into differently phase-encoded stimulated echoes. Because PPA versions shorten the train of stimulated echoes, they enable higher flip angles and hence proportionally increase the signal strength of the individual echoes. Thus, the resulting images not only possess shorter acquisition times but also higher SNR as recently confirmed in preliminary implementations [53, 54].

4. MRI contrasts

Apart from being noninvasive, a major advantage of MRI in comparison with x-ray computed tomography (CT), positron emission tomography (PET), or single photon emission computed tomography (SPECT) is the large variety of different soft tissue contrasts.

4.1. Spin density, T_1, and T_2 contrast

Figure 11 shows representative MRI sections of the human brain with spin density, T_1, T_2, and $T_2^\star$ contrast. In spin density-weighted MRI, the image intensity is dominated by differences in the water content of the tissue. Accordingly, in the CNS, white matter structures appear darker than grey matter due to a lower water content. On the other hand, the cerebrospinal fluid (CSF) within the ventricles presents with high signal intensities. Using short echo times, spin density contrast can be obtained either with spin-echo sequences and repetition times which are large compared to T_1 (e.g., $\geqslant$3000 ms) or with FLASH sequences and flip angles much smaller than the Ernst angle

$$\alpha_E = \arccos(\exp(-\mathrm{TR}/T_1)). \tag{11}$$

Conversely, T_1 contrast is best obtained with FLASH sequences and flip angles larger than the Ernst angle, so that white matter, which has a shorter T_1 than grey matter, appears bright compared to cortical grey matter. Because of the very long T_1 relaxation time of CSF, the ventricles exhibit very low intensities.

T_2 contrast is accomplished with (fast) spin-echo sequences using effective echo times of the order of T_2 (e.g., 50–100 ms) and long repetition times which avoid

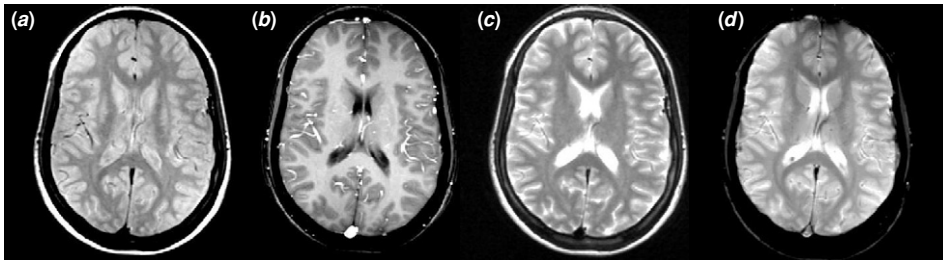

Figure 11. Transverse sections of the human brain using (*a*) spin density, (*b*) T_1, (*c*) T_2 and (*d*) $T_2^\star$ contrast (2.0 T). The images are reconstructed from a 3D data set with a spatial resolution of $1 \times 1 \times 1$ mm^3.

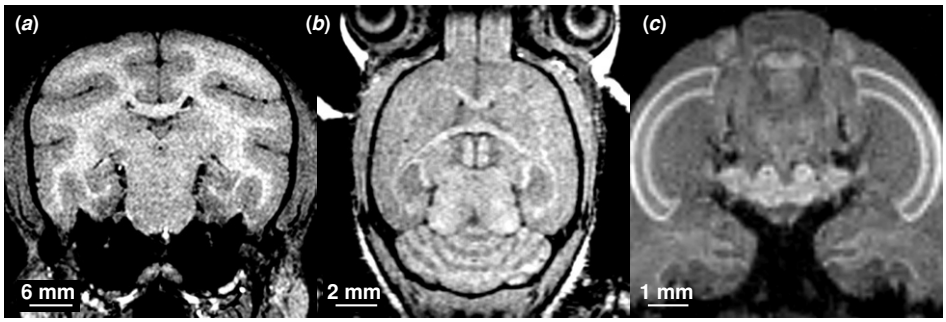

Figure 12. Selected sections from T_1-weighted 3D MRI *in vivo* (2.35 T) of the brain of (*a*) a squirrel monkey (acquired voxel size $310 \times 310 \times 310$ μm^3), (*b*) a mouse ($117 \times 117 \times 156$ μm^3), and (*c*) an insect (sphinx moth *Manduca Sexta*) in the pupal state ($100 \times 100 \times 100$ μm^3).

residual T_1 weighting. Because the pronounced sensitivity of T_2 relaxation times to pathological alterations generally causes well-identifiable hyperintensities, T_2 contrast is the most frequently used parameter in clinical diagnostics for the detection of brain disorders (e.g., atrophy, inflammation, neurodegeneration).

When moving from a spin-echo to a gradient-echo sequence, the decay of the gradient-echo signal intensity with time not only reflects the true T_2 relaxation but also the presence of magnetic field inhomogeneities, that is a certain degree of intravoxel signal dephasing due to the mutual cancellation of off-resonance contributions. The correspondingly shorter effective spin–spin relaxation time $T_2^\star$ dominates the contrast properties of, for example, EPI. $T_2^\star$-weighted images may also be obtained by using FLASH sequences with a long echo time of the order of $T_2^\star$, for example, about 30 ms for brain tissue at 3 T. $T_2^\star$-sensitive imaging sequences are the basis for monitoring differences in the blood oxygenation level dependent contrast, which is central to studying the functional organization of the human brain by mapping differences in brain activity (see section 5.2).

Extending clinical applications and research devoted to human neuroscience, high-resolution MRI may be scaled down to smaller brains. Despite the necessary increase in the absolute spatial resolution, similar experimental conditions may be retained if the lower SNR from the smaller voxels can be compensated for by the use of optimized RF coils. This mainly refers to receive-only surface coils the size of which matches the desired FOV. Accordingly, figure 12 demonstrates that brain images of comparable quality to human studies may be obtained from a variety of species ranging from primates to rodents and even insects.

With respect to their role in system-oriented neurobiology of genetically engineered animals, MRI studies of mouse brain are of particular importance. However, special attention has to be paid to adapt the spatial resolution to the size of the anatomic structures of interest. Figure 13 demonstrates how unreasonably thick MRI sections obscure anatomic details by merging signal intensities from neighbouring though distinct structures, for example see images with section thicknesses of 500 μm or more in the left two columns of figure 13. While coarse structures such as the cerebellum, midbrain and olfactory bulb are readily visible even with a section thickness of 1000 μm, at least 500 μm sections are required to resolve major white matter tracts such as the corpus callosum, external capsule and hippocampal fimbria. A further decrease to 234 μm or 156 μm reveals even smaller structures such as the hippocampal formation and the medial habenular nuclei in the right two columns of figure 13. These findings favour the use of an isotropic spatial resolution for MRI of small brains. For mice such strategies lead to a desirable linear voxel dimension of about 100 μm.

4.2. Exogenous contrasts

The use of an exogenous contrast agent that modulates the water proton relaxation properties of the system under investigation has already been suggested by Lauterbur in his first MRI publications [1, 56]. The most obvious targets are water-soluble paramagnetic ions that carry unpaired electrons. Their main effect is twofold: a shortening of the T_1 relaxation times of neighbouring water protons, and a disturbance of the local (microscopic) magnetic field homogeneity which in turn shortens the $T_2^\star$ values of affected water protons.

Clinical applications may benefit from the administration of a contrast medium by adding dynamic functional information. The prototypes of well-approved human contrast agents are gadolinium chelates which maintain the pronounced

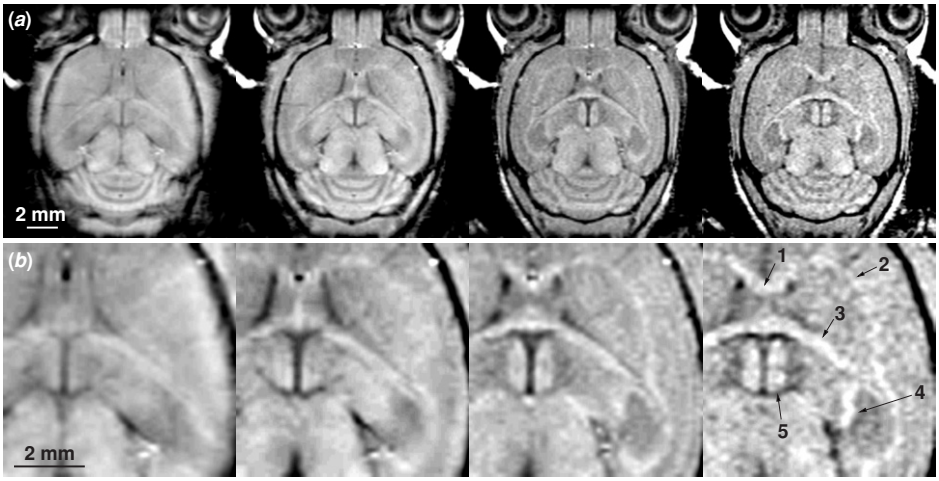

Figure 13. T_1-weighted 3D MRI of mouse brain *in vivo* (2.35 T) at 117 × 117 μm^2 in-plane resolution. (*a*) Selected horizontal sections and (*b*) magnified views demonstrate enhanced soft-tissue contrast and reduced partial volume effects for section thicknesses decreasing from (left) 938 μm to 469 μm, 234 μm, and (right) 156 μm. (1) Corpus callosum, (2) external capsule, (3) hippocampal fimbria, (4) hippocampal formation and (5) medial habenular nucleus. Adapted from [55].

relaxivity of Gd^{3+} in the organic complex while reducing the toxicity of the free ion by several orders of magnitude [57]. In the CNS the complex also prevents the ion passing the blood–brain barrier (BBB) after intravenous injection. Thus, Gd chelates are commonly used to monitor a breakdown of the BBB by a focal enhancement of T_1-weighted images after leakage of the contrast agent into the (pathological) brain tissue.

The application of uncomplexed free ions such as Mn^{2+}, for example in the form of an aqueous solution of $MnCl_2$, is restricted to animal studies. Manganese is attractive for functional mapping of fibre tracts *in vivo* because Mn^{2+} ions can be taken up by excitable neurons through voltage-gated divalent cation channels as an analogue to Ca^{2+} [58, 59]. Subsequent to neuronal uptake, the ions are actively transported from the cell body along the axons [60, 61]. This behaviour can be exploited for a delineation of the axonal connectivity and a determination of the functional relevance of selected fibre tracts *in vivo* [62–64]. Furthermore, a systemic administration of manganese may be used as an *in vivo* staining technique for several functional and morphologic aspects of the brain [65].

Another class of contrast agents is based on small ferromagnetic particles which effectively disrupt the focal magnetic field homogeneity and therefore lead to signal cancellations in $T_2^\star$-weighted images. These contrast agents are classified as superparamagnetic particles of iron oxide (SPIO), ultrasmall superparamagnetic iron oxide (USPIO) and monocrystalline iron oxide nanoparticles (MION). Upon binding to a target molecule (e.g., a receptor or antibody) or after labelling of specific cells, magnetic contrast agents are expected to become 'intelligent' markers of important biologic or disease processes. For example, preliminary studies have marked and tracked the migration of macrophages [66] and stem cells [67] within the CNS.

4.3. Physiological motions and beyond

Several MRI contrasts refer to signal changes which are induced by the different physical properties of stationary and moving spins and their respective interferences with the image acquisition process. Of course, macroscopic motion such as involuntary subject movements poses a basic problem for MRI when occurring during imaging.

Motion not only affects the dynamic steady-state equilibrium magnetization and therefore causes amplitude variations during coverage of *k*-space, but also leads to phase errors in the image raw data. This is because motion-induced phase shifts which are caused by spin displacements in the presence of a magnetic field gradient add to the phase information acquired during spatial encoding. As a consequence, FT of such contaminated image data results in geometric errors along the phase-encoding dimension of the image which typically occur as smearing or ghosting artefacts depending on the nature (e.g., periodicity) of the movements.

Nowadays, subject movements due to pulsatile flow and respiration are either controlled by suitable gating schemes or minimized by spatial presaturation, higher-order gradient compensation schemes, or high-speed imaging in conjunction with breathholding.

4.3.1. Angiography. Physiological motions of water protons refer to (coherent) vascular flow and (incoherent) tissue perfusion and represent important medical information. Marked signals from (rapidly) flowing spins in vessels crossing the imaging volume were first identified as inflow effects in gradient-echo MRI [68] shortly after invention of the FLASH principle. Corresponding time-of-flight magnetic resonance angiography (MRA) techniques exploit the continuous refreshment of previously unsaturated spins that reach the image section. These spins yield a much higher MRI signal than stationary spins within the image section because the latter are in a pre-saturated steady state after multiple RF pulses from preceding excitations.

Arbitrarily oriented angiograms are obtainable from 3D MRI acquisitions by suitable post-processing algorithms using maximum intensity projections. As illustrated by the high-quality angiogram of the human intracranial vasculature in figure 14, current implementations of 3D gradient-echo MRI

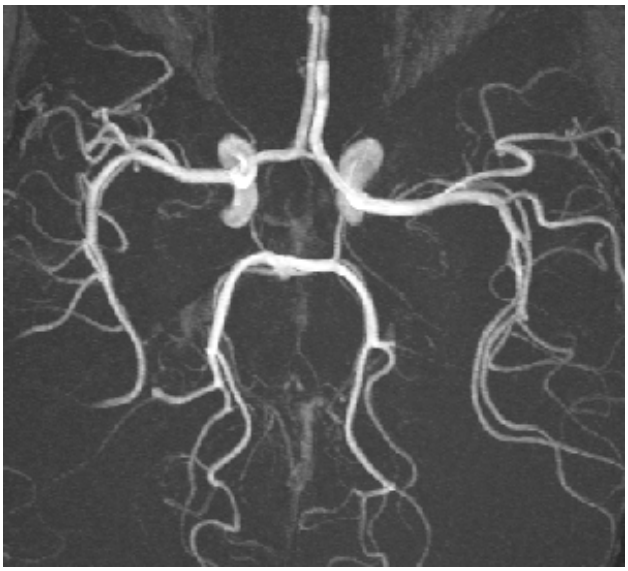

Figure 14. Magnetic resonance angiogram (transverse view) of the human brain *in vivo* (2.9 T). The map corresponds to a maximum intensity projection of a T_1-weighted flow-sensitized 3D MRI data set acquired at $0.28 \times 0.56 \times 0.8$ mm^3 resolution (3D FLASH, TR/TE = 40.0/3.84 ms, flip angle 25°).

sequences are capable of not only emphasizing inflow effects but also minimizing putative signal void due to turbulence by using very short echo times.

Inflow or time-of-flight MRA approaches are complemented by phase-contrast MRA techniques that exploit the phase differences between flowing and stationary spins [69, 70]. More precisely, while stationary spins that are subjected to two sequential magnetic field gradients of opposite polarity fully refocus their macroscopic magnetization in an echo, part of this signal is dephased for flowing spins. In fact, the phase accumulated in the presence of the gradients is directly proportional to the velocity. The flow-related phase information may therefore be used for angiographic mapping as well as for quantitative measurements of flow velocities. In comparison with time-of-flight techniques, phase-contrast MRA has advantages in mapping slow flow including CSF flow. For an overview of angiographic MRI techniques and their applications to human brain, see [71–74].

4.3.2. Perfusion. Transport of water protons in the capillary bed of the microvasculature is usually described as parenchymal tissue perfusion. These processes are accessible by MRI and, together with the apparent diffusion coefficient (ADC) in tissue (see below), provide important clinical information in a variety of brain disorders (e.g. see [75, 76]).

The most robust technique for perfusion imaging is based on the dynamic monitoring of the first pass of a paramagnetic contrast agent through the tissue. Bolus tracking is accomplished by means of a susceptibility-sensitized (or $T_2^\star$-weighted) high-speed MRI sequence such as EPI which offers multi-slice coverage of the brain with a temporal resolution of about 1–2 s. Immediately after a rapid injection of, for example, Gd-DTPA the high vascular concentration of the paramagnetic complex causes magnetic field disturbances that dephase the signal of surrounding water protons and shorten the $T_2^\star$ value [77]. Accordingly, proper perfusion of brain tissue is indicated by a reversible signal decrease with a mean duration of about half the blood circulation time in the body, i.e. about 10–15 s in humans. The previously described T_1-shortening effect of Gd-DTPA requires a more dilated distribution of the contrast agent and therefore takes a few minutes after administration to fully develop.

As an alternative to the use of exogenous contrast agents, the inflow approach used for MRA may also be adjusted to the conditions of a flow-related enhancement by perfusion. The prototype sequence has been described by Detre *et al* [78] who continuously saturated (or inverted) arterial water protons in the neck before they entered the brain. Because of the RF tagging pulses that manipulate the amplitude of inflowing spins, pertinent techniques are also termed arterial spin labelling (ASL). Although quantitative measurements of cerebral blood flow in units of ml/100 g tissue/min are complicated by a number of corrections for T_1 relaxation and magnetization transfer effects, numerous variants and improvements have been reported in recent years. Their discussion remains outside the scope of this review.

4.3.3. Diffusion. Complementing flow and perfusion studies, diffusion-weighted MRI allows for an assessment of the microscopic mobility and translational motion of water protons in tissue. In 1965, well before the advent of MRI, Stejskal and Tanner [79, 80] described a method for the encoding of diffusion properties into the spin-echo signal and a determination of the molecular self-diffusion coefficient. The corresponding scheme is shown in figure 15 where G_0 and δ represent the amplitude and duration of the diffusion-encoding gradients, respectively, and Δ the diffusion time. Only hypothetical spins that remain stationary during the application of the gradient pair achieve a full refocusing of the spin echo. In contrast, spins that move to a different location—and therefore experience a different field strength during the refocusing period—become partially dephased. The corresponding decrease of the net macroscopic magnetization increases with the diffusion coefficient D as well as with G_0, δ and Δ. The analysis reveals that the spin-echo intensity decreases exponentially according to

$$\frac{M(t)}{M_0} = \exp(-bD) \tag{12}$$

with

$$b = \gamma^2 G_0^2 \delta^2 \left(\Delta - \tfrac{1}{3}\delta\right). \tag{13}$$

The diffusion coefficient may therefore be obtained by measuring the spin-echo amplitude as a function of gradient strength, that is for different b values.

Multiple trials have been undertaken to combine the Steijskal–Tanner approach with imaging. Even for the CNS, the key problem for *in vivo* studies is small phase distortions caused by unavoidable tissue (or organ) motions, for example due to respiratory movements or pulsatile flow. Today, the only practical solution for diffusion imaging is the combination of a diffusion-encoding spin-echo preparation module with a high-speed imaging sequence that spatially encodes the spin-echo signal in a subsequent readout scheme. In principle, the idea can be realized with almost any single-shot MRI

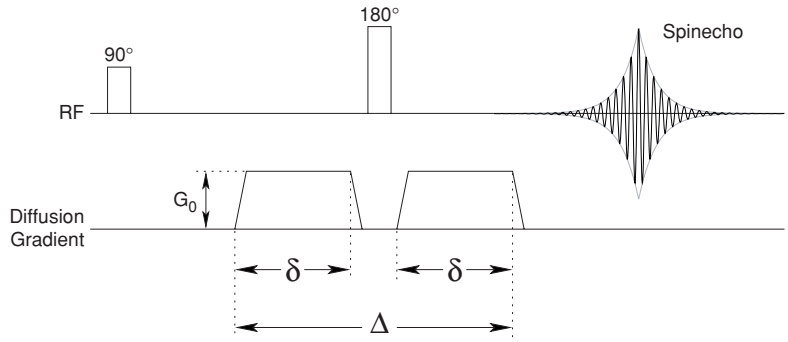

Figure 15. Diffusion-encoding spin-echo sequence as originally proposed by Stejskal and Tanner [79, 80]. The method depends on the incomplete refocusing of signals from spins moving during the application of the balanced pair of self-compensating diffusion gradients. While stationary spins remain unaffected, moving spins give rise to a signal loss which increases with gradient strength and molecular self-diffusion coefficient.

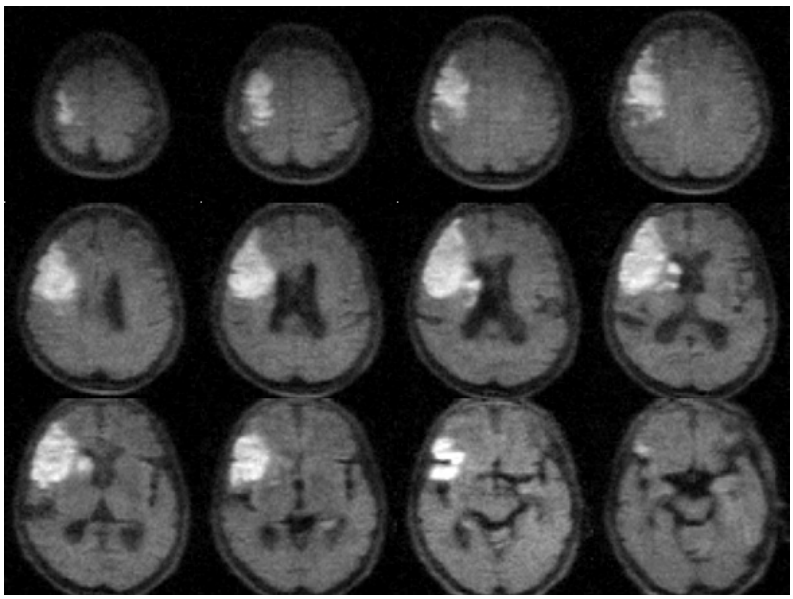

Figure 16. Isotropic diffusion-weighted maps of a patient with acute stroke (1.5 T, contiguous sections of 6 mm thickness and 2×2 mm^2 in-plane resolution). Ischaemic lesions present with a reduced ADC value and therefore appear bright on diffusion-weighted images. The diffusion-weighted single-shot STEAM MRI sequence is insensitive to susceptibility differences and geometric distortions.

technique, although so far most approaches use EPI readout gradients.

An obvious disadvantage of diffusion-weighted EPI is the unwanted sensitivity to susceptibility differences and the occurrence of related image artefacts. An alternative approach is therefore the use of a (half Fourier) single-shot STEAM MRI sequence [13, 51], which employs RF refocused stimulated echoes that eliminate off-resonance effects. In this case, the first 90° RF pulse of the 90°–90°–(α–TR)$_n$ sequence which normally excites the transverse magnetization is replaced by the spin-echo of the Stejskal–Tanner 90°–180°–SE sequence [81]. The major advantage of diffusion-weighted single-shot STEAM MRI is the complete lack of susceptibility problems, the absence of geometric distortions and the resulting spatial congruence with high-resolution anatomic MRI scans. The slight penalty in SNR relative to EPI is expected to be compensated for by combinations with parallel acquisition techniques as discussed in a preceding section [13].

In terms of applications, it was early noted that the cerebral ADC depends on the cellular ion and water homeostasis of the tissue. In particular, because of the breakdown of the energy metabolism in affected cells, the water apparent diffusion is significantly slower in regions of acute ischaemia compared with normal brain tissue [75]. These observations in experimental animals and later in patients render diffusion-weighted MRI the most important tool for the early diagnosis of stroke (e.g. see [82, 83]). Figure 16 demonstrates the 'lightbulb' effect of a reduced ADC which highlights ischaemic regions in a patient with acute stroke.

4.3.4. Magnetization transfer. Finally, access to the pools of (partially) immobilized—and under MRI conditions invisible—protons provides another MRI contrast [84, 85]. It is caused by an indirect transfer of saturated magnetization from immobilized protons to the pool of MRI-detectable mobile water protons.

As illustrated in figure 17, the interaction involves a direct dipolar coupling as well as proton and water exchange between semisolid macromolecular protons and bulk water protons. Most likely, the *in vivo* magnetization transfer (MT)

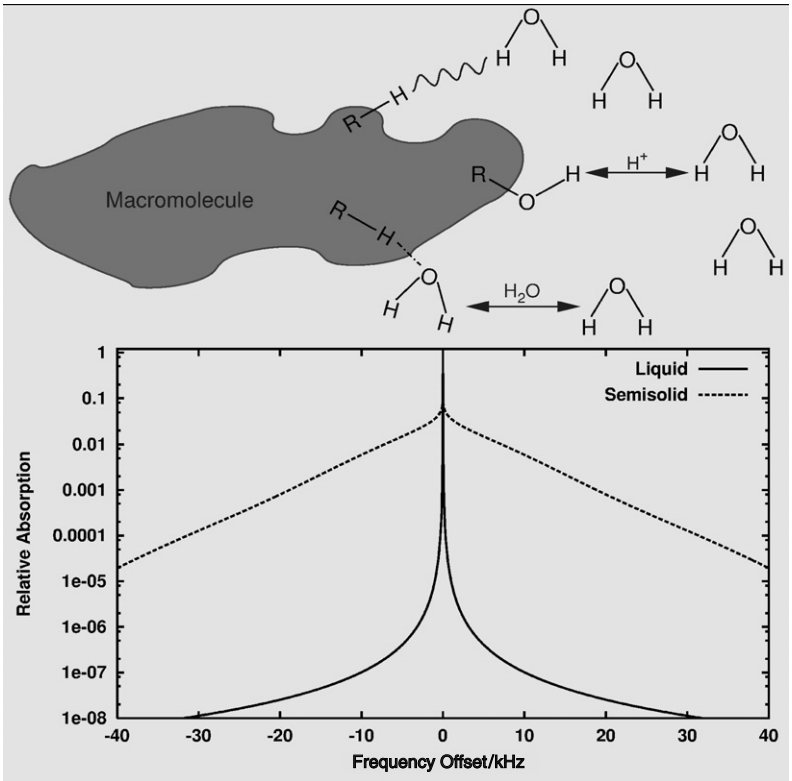

Figure 17. (Top) The mechanisms underlying magnetization transfer contrast comprise interactions between mobile water protons and (partially) immobilized or bound protons via direct dipolar couplings, proton exchange and water exchange. (Bottom) The resonance lines of semisolid protons are much broader than those obtained for mobile protons (Lorentzian lineshape) and may therefore be selectively saturated by off-resonance irradiation.

contrast predominantly relies on hydroxyl protons bound to the surface of intracellular macromolecules. Because the resonance lines for bound protons are much broader than the Lorentzian lineshape of a water proton, it is possible to saturate the pool of semisolid protons by off-resonance irradiation without a direct contamination of mobile protons. Thus, a transfer of the saturated magnetization to the MRI-detectable protons is only possible via the aforementioned mechanisms. Or conversely, the observation of an MRI signal attenuation in response to off-resonance irradiation, that is the occurrence of MT contrast, indicates the presence of a significant amount of macromolecular structure in the respective tissue.

Human applications of MT contrast are mainly in the field of multiple sclerosis and in angiography where the additional MT attenuation of the stationary tissue signal further enhances the vascular contrast. More recently, Natt *et al* [55] described the use of MT contrast in studies of rodent brain. As shown in figure 18 the technique helps to discriminate densely packed grey matter in the mouse hippocampal CA3 region (pyramidal cell layer) from normal white matter in the hippocampal fimbria and external capsule.

5. Advanced applications

The two most relevant advances in MRI of the human brain address the functional properties of grey and white matter in the intact CNS. While neural systems in grey matter are primarily concerned with information processing, white matter represents bundles of myelinated axons interconnecting such functionally specialized cortical and subcortical areas. Both elements may nowadays be visualized by MRI using either blood oxygenation level dependent (BOLD) contrast for mapping brain function or directional diffusion information about the molecular water mobility for 3D tracking of nerve fibre bundles. Together, such techniques expand the list of MRI applications to the functional diagnosis of neurological and psychiatric dysfunction and the monitoring of cortical reorganization and neurorehabilitation.

5.1. Tractography: diffusion tensor mapping of axonal connectivity

In the complex structures forming brain tissue, the diffusion of water molecules is restricted by membranes. Accordingly, the ADC decreases from its value in bulk water with increasing diffusion time Δ (compare figure 15), if—for a given diffusion coefficient—Δ is long enough for water molecules to reach the boundaries of a confined compartment. In the CNS typical ADC values of grey and white matter are about 0.7×10^{-3} mm^2 s^{-1}. Thus, in order to avoid motional restrictions, diffusion MRI studies are commonly performed with diffusion times of the order of 20 to 30 ms [86].

A second more important property of water diffusion in tissue is the microscopic anisotropy of the translational mobility. It is primarily encountered in white matter which favours intracellular water diffusion (or transport) along the myelinated axons but not perpendicular to the fibre direction, that is across the axonal membrane and the surrounding myelin

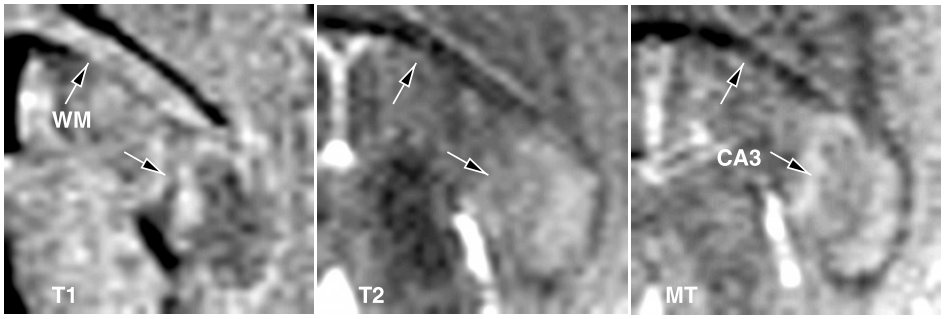

Figure 18. T_1, T_2 and magnetization transfer (MT) contrast of the mouse hippocampus *in vivo* (2.35 T). MT contrast distinguishes densely packed grey matter in the CA3 region of the hippocampus from white matter (WM). Otherwise, both the CA3 region and white matter in the hippocampal fimbria appear either bright (T_1) or dark (T_2). Adapted from [55].

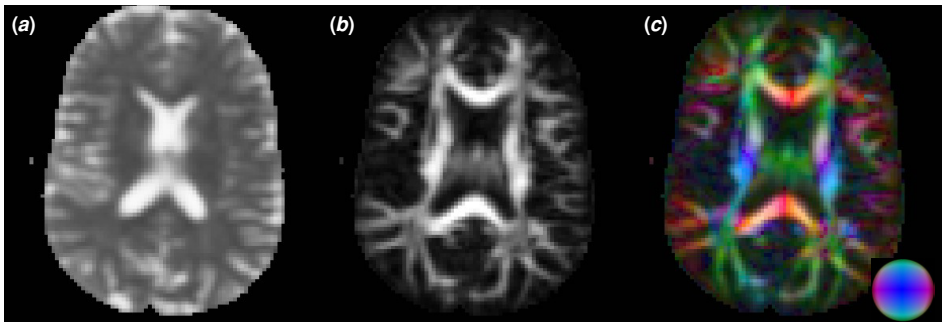

Figure 19. Diffusion tensor maps of the human brain (2.9 T, single-shot STEAM MRI, 24 gradient orientations, $b = 1000$ s mm^{-2}, 2 mm isotropic resolution). (*a*) Isotropic ADC with bright intensities indicating high diffusion in CSF. (*b*) Fractional anisotropy with bright intensities indicating pronounced anisotropy in white matter. (*c*) Colour-coded mean diffusion direction with orientations as indicated (red: right–left, blue: head–foot, green: anterior–posterior).

sheaths. Anisotropic diffusion may easily be probed by MRI using diffusion-encoding gradients along selected directions. The effects in white matter were first observed in cat brain by Moseley *et al* [87] and later verified in humans by Chenevert *et al* [88]. Measurements of the orientational dependence of the ADC may therefore be exploited to determine the orientation of fibre bundles in the intact brain [89–91].

A simple vectorial description of diffusion NMR experiments may be achieved by extending the phenomenological Bloch equation (4) by an additional term to the Bloch–Torrey equation [79, 92]

$$\frac{\mathrm{d}}{\mathrm{d}t}\boldsymbol{M} = \gamma \boldsymbol{M} \times \boldsymbol{B}_1 + \boldsymbol{R}\boldsymbol{M} + \begin{pmatrix} 0 \\ 0 \\ 1/T_1 \end{pmatrix} M_0 + \boldsymbol{\nabla} \cdot (\boldsymbol{D}\boldsymbol{\nabla}\boldsymbol{M}) \tag{14}$$

where $\boldsymbol{D}$ corresponds to the diffusion tensor. The diffusion term yields an additional loss of transverse magnetization given by

$$\frac{M(t)}{M_0} = \exp\left(\int_0^t \boldsymbol{k}(\tau)^T \boldsymbol{D}\boldsymbol{k}(\tau)\,\mathrm{d}\tau\right), \tag{15}$$

with $\boldsymbol{k}(\tau)$ the $\boldsymbol{k}$ space position according to equation (9). Assuming a symmetric diffusion tensor $D_{ij} = D_{ji}$, the signal attenuation can be expressed as a simple exponential

$$\frac{M(t)}{M_0} = \exp\left(\sum_{i,j=1}^{3} b_{ij}(t) D_{ij}\right) \tag{16}$$

where the b value also represents a matrix according to

$$b_{ij}(t) = \exp\left(\int_0^t k_i(\tau) k_j(\tau)\,\mathrm{d}\tau\right). \tag{17}$$

Most diffusion MRI studies of the brain favour the diffusion tensor model [93] outlined above. The diffusion tensor can be estimated from equations (16) and (17) by a minimum of six measurements with linearly independent b matrices and one acquisition without diffusion weighting.

Several scalar invariants [94] are commonly in use for a visual presentation of the diffusion tensor data. An important parameter is the trace of the diffusion tensor or isotropic ADC (see also figure 19(*a*)) which is frequently used for diagnostic purposes. Other invariants such as the relative anisotropy (RA) or fractional anisotropy (FA) clearly distinguish grey matter with an almost isotropic diffusion from white matter. The pronounced anisotropy in white matter is clearly demonstrated in figure 19(*b*). In addition, figure 19(*c*) presents a colour-coded visualization of the mean diffusion direction (MDD) which corresponds to the principal axis of the diffusion tensor with the largest eigenvalue. (Figures 19–23 appear in colour in the electronic version of this journal.)

Various methods have been proposed [90, 91] to exploit this directional information for an analysis of axonal connectivity in the brain. The idea is to track individual fibre bundles by linking neighbouring voxels in a 3D acquisition according to their MDD. For the example shown in figure 20, fibre tracks were calculated with the simple but robust FACT algorithm [90]. Criteria for termination of the iterative process which adds neighbouring pixels according to their directional similarity include an anisotropy threshold and a maximum

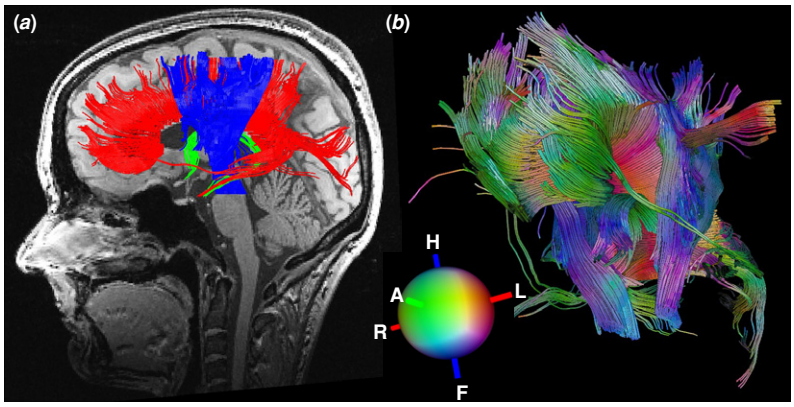

Figure 20. MR tractography of the human brain based on diffusion tensor mapping (parameters as in figure 19). (*a*) Fibre tracts running through the corpus callosum (red), the fornix (green) and the posterior part of the internal capsule (blue) viewed in front of a sagittal section (T_1-weighted 3D MRI). (*b*) Corresponding 3D view with colours corresponding to the mean diffusion direction as indicated (RL: right–left, HF: head–foot, AP: anterior–posterior). Courtesy of M Küntzel.

stiffness condition. In contrast to conventional histological preparations, the *in vivo* MRI information is of an intrinsic 3D nature and therefore requires proper visualization tools. In this respect figure 20 shows only a single selected 3D view of the neuronal tracts passing through the corpus callosum, fornix and internal capsule with colours referring to the local fibre directions.

It is fair to note that the diffusion tensor approach does not completely describe the structural information available by diffusion-weighted MRI. This is particularly true for white matter areas where different fibre bundles are crossing. The underlying distribution of diffusional directions cannot be modelled by a simple ellipsoid. Different approaches such as diffusion MRI at high angular resolution [96] and q-space methods [97] are currently under evaluation to circumvent the restrictions of the tensor model.

5.2. *Mapping of human brain function*

The BOLD contrast was discovered by Ogawa and colleagues in high-field gradient-echo MRI of rat brain [98]. Under these conditions the venous vasculature resulted in dark structures within brain images which could be explained by the high intravascular concentration of deoxyhaemoglobin. In contrast to the diamagnetic oxyhaemoglobin complex, deoxyhaemoglobin is a paramagnetic molecule which acts as an endogenous contrast agent for $T_2^\star$-weighted gradient-echo MRI. Thus, BOLD MRI signal changes are primarily due to deoxyhaemoglobin-related susceptibility effects which alter the microscopic magnetic field gradients in and around capillaries, venules and veins. This understanding of the BOLD contrast offers its use as a dynamic indicator of activation-induced changes in cerebral blood flow and metabolism which accompany the neural processing of a functional challenge as first demonstrated in humans in 1992 [99–102].

Basically, BOLD MRI of brain function relies on a perfusion-mediated indirect measure of changes in neural activity. The current 'consensus model' of the mechanisms underlying the haemodynamic response to increased brain activity first involves a major increase in focal cerebral blood flow. The concomitant excess delivery of oxyhaemoglobin emerges as the predominant parameter for MRI because it effectively decreases the absolute deoxyhaemoglobin concentration in the venous part of the microvasculature. The resulting MRI signal increase (less dephasing) is only partly counterbalanced by a slight increase of the deoxyhaemoglobin level arising from enhanced oxygen consumption and increased cerebral blood volume. Taken together, the net balance yields an increase of the MRI signal upon functional activation.

An important point to emphasize is the fact that functional MRI detects *changes* of brain activity rather than brain activity *per se*. As a consequence, the approach does not allow for an absolute quantitation of brain activity. Instead, serial MRI recordings attempt to identify relative differences between successive functional states of the subject under investigation. Typically, multislice EPI offers coverage of the entire brain with a temporal resolution of 2–3 s. In the simplest case, a protocol for functional MRI alternates between an activated state, in which the subject has to perform a certain task, and a control state which may be a 'resting' state or a slightly different task. Afterwards, the time courses of the MRI signal intensity changes in each individual voxel are correlated with a reference function which mimics the protocol (e.g., a boxcar function with 1 during activation and 0 during control). The correlation coefficients are then a measure of the strength of activation in the corresponding voxel. Colour-coded activation maps may be obtained after proper statistical analyses as, for example, described by Baudewig *et al* [103].

The example shown in figure 21 relates to the retinotopic organization of the visual cortex, that is the encoding of ordered and spatially segregated representations of different parts of the visual field on the surface of the occipital lobe. The paradigm consists of 10 s presentations of six rings with increasing diameter (stimuli as insets) expanding over the subject's visual field from its centre to the periphery. During data analysis each ring stimulus was contrasted with all other stimuli which resulted in differential representations for the various parts of the visual field with increasing eccentricity. Thus, the same data set was analysed multiple times with different boxcar reference functions each selecting a particular stimulus.

The choice of spatial resolution is an important issue in planning a functional MRI study of human brain activation. During data acquisition the voxel size determines the SNR,

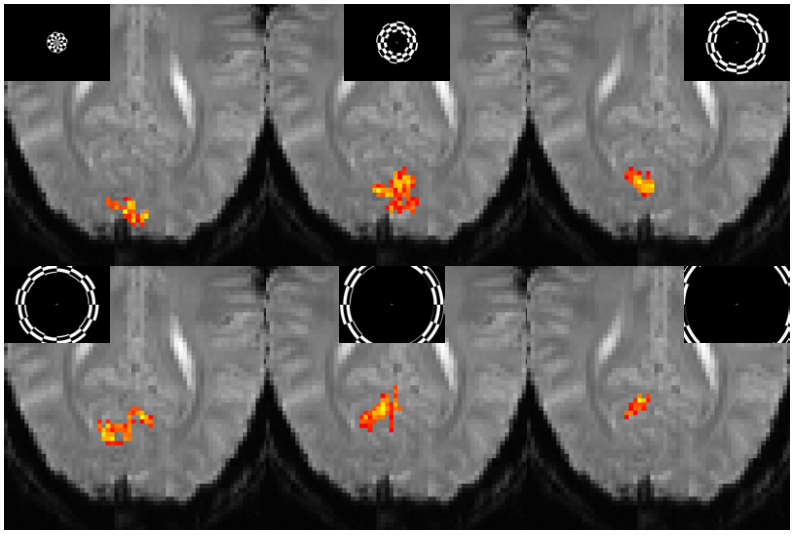

Figure 21. Functional MRI (2.0 T) of the retinotopic organization of the human visual cortex (eccentricity). The paradigm consists of six successive 10 s presentations of rings with increasing diameter (insets) expanding over a $30^\circ \times 40^\circ$ visual field. Within the same image section, the colour-coded activations move from the occipital pole (representation of the fovea: central viewing) into more anterior locations (peripheral viewing). Adapted from [95].

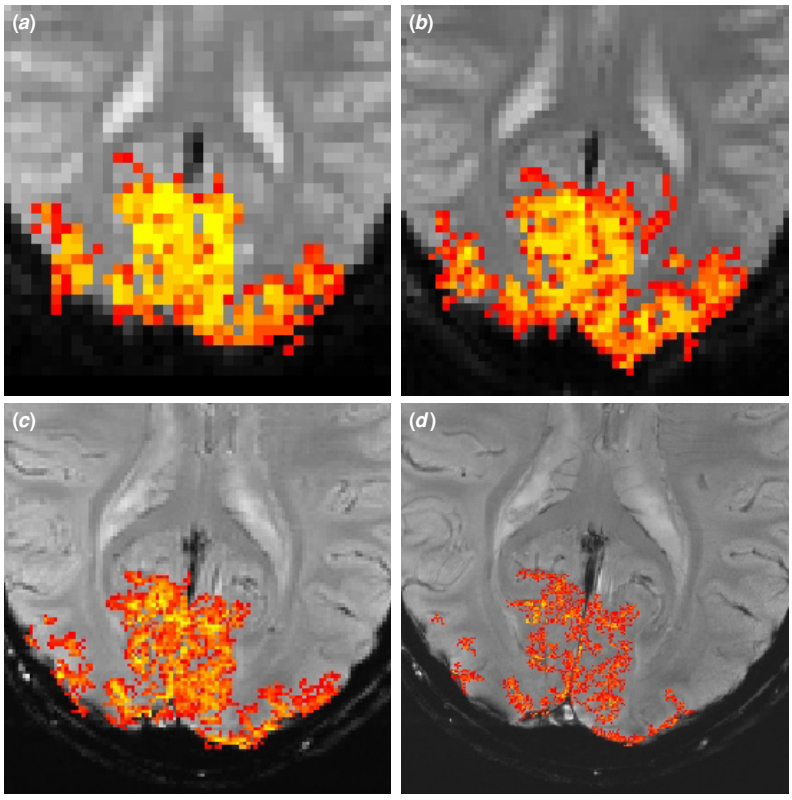

Figure 22. Functional MRI of the visual cortex as a function of spatial resolution (2.9 T). (*a*) EPI at 3 mm and (*b*) 2 mm in-plane resolution as well as (*c*) multi-echo FLASH MRI at 1 mm and (*d*) 0.5 mm resolution (4 mm sections). A reduction of the voxel size minimizes partial volume effects with nonactivated tissue and thereby restricts activations to cortical grey matter at the expense of reduced SNR.

the functional contrast-to-noise ratio (CNR), and the degree of susceptibility-induced signal losses and geometric distortions. Thus, apart from merely blurring or resolving activations within the brain system under investigation, the experimental acquisition parameters have additional influence on the outcome of the mapping study. For example, low spatial resolution may completely hamper the detectability of brain regions close to air–tissue interfaces or compromise the CNR by partial occupation with non-activated tissue (i.e., white matter) to such a degree that it affects the correlation analysis. Moreover, during post-processing, the use of spatial (or temporal) filtering as well as the transformation of activation maps into a standardized brain atlas for intersubject averaging may further compromise the results.

Figure 22 compares visual activation maps obtained as a function of spatial resolution. While voxel dimensions

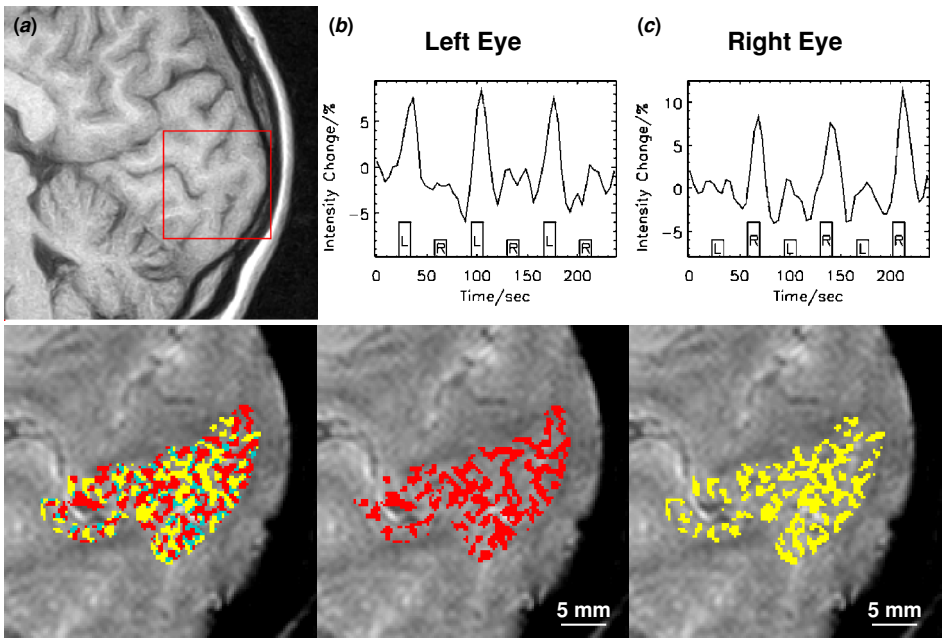

Figure 23. Ocular dominance columns in human primary visual cortex (2.0 T, multi-echo FLASH, 0.5 × 0.5 mm^2 resolution interpolated to 0.25 × 0.25 mm^2, 4 mm section). (*a*) Anatomical section covering the striate cortex and (bottom) overlay of separate BOLD MRI activation maps obtained for monocular stimulation of the left eye (red) and right eye (yellow). The absence of a substantial number of overlapping voxels (blue) confirms the identification of spatially segregated functional units predominantly coding for an individual eye. (*b*), (*c*) The middle and right parts of the figure show (top) BOLD MRI signal intensity time courses and (bottom) corresponding activation maps of responses elicited by left and right eye stimulations, respectively. Adapted from [95].

of 3 mm to 4 mm yield considerable blurring relative to the structures detectable in high-resolution anatomical scans, an in-plane resolution of 2 mm allows for a more adequate mapping of the gross functional organization of most brain systems. On the other hand, an unambiguous restriction of activations to cortical grey matter is only achieved for a spatial resolution of 1 mm. Here, single-shot EPI had to be replaced by a multi-echo FLASH sequence [104] which maintains BOLD sensitivity at the expense of volume coverage for a given temporal resolution. In the extreme case of 0.5 mm the acquisition had to be reduced to a single section with additional compromises in SNR.

So far, the exceptional potential of BOLD MRI at very high spatial resolution has mainly been exploited for mapping the columnar organization of the primary visual cortex [104–107]. The largest structures of such functional units refer to the separate processing of incoming information from either the left or right eye. In human striate cortex these elements form neighbouring columns of cortical grey matter with a diameter of 0.75 mm to 1.0 mm. As shown in figure 23 monocular stimulation indeed results in pronounced BOLD MRI signal intensity changes which reflect neural activity specific for a single eye [104]. The approach yields spatially distributed activations for individual eye representations that closely resemble the neuroanatomical observations of 'frequent bifurcations, blind endings, and islands' found in combined serial sections of specimens from patients blind in one eye [108].

6. Outlook

MRI has passed through a tremendous development since its inception in 1973. Nowadays, most of the imaging techniques discussed in this review are readily available to both neurologists and neurobiologists for patient care or neurobiological research. In fact, the potential of this technology to bridge the gaps between genomics, animal models and clinical diagnostics is of utmost importance. Foreseeable developments include the use of 'intelligent' contrast agents based on magnetic nanoparticles which are bound to functional units such as antibodies or receptors. Technically, parallel acquisition techniques with acceleration factors of about 10–20 will push MRI further to the limits and provide unique new opportunities. Appropriately modified MRI sequences will open the way for even higher spatial and/or temporal resolution, reduced sensitivity to artefacts and in some cases even better SNR.

References

[1] Lauterbur P C 1973 Image formation by induced local interaction: examples employing nuclear magnetic resonance *Nature* **242** 190–1
[2] Dixon R L and Ekstrand K E 1982 The physics of proton NMR *Med. Phys.* **9** 807–18
[3] Abragam A 1978 *The Principles of Nuclear Magnetism* (Oxford: Oxford University Press)
[4] Bloch F, Hansen W W and Packard M 1946 Nuclear induction *Phys. Rev.* **69** 127
[5] Hahn E L 1950 Spin echoes *Phys. Rev.* **80** 580–94
[6] Haase A, Frahm J, Matthaei D, Merboldt K D and Hänicke W 1986 FLASH imaging: rapid NMR imaging using low flip angle pulses *J. Magn. Reson.* **67** 258–66
[7] Frahm J, Haase A and Matthaei D 1986 Rapid three-dimensional MR imaging using the FLASH technique *J. Comput. Assist. Tomogr.* **10** 363–8
[8] Pauly J, Nishimura D and Macovski A 1989 A *k*-space analysis of small-tip-angle excitation *J. Magn. Reson.* **81** 43–56

[9] Rieseberg S, Frahm J and Finsterbusch J 2002 Two-dimensional spatially-selective rf excitation pulses in echo-planar imaging *Magn. Reson. Med.* **47** 1186–93
[10] Kiefer B and Hausmann R 1993 Fast imaging with single-shot MR imaging techniques based on turbo SE and turbo GSE *Radiology* **189** 289
[11] Kiefer B and Kolem H 1994 Imaging the abdomen in a single breathhold 2-shot HASTE *Proc. Soc. Magn. Reson.* **2** 481
[12] Jesmanowicz A, Bandettini P and Hyde J S 1998 Single-shot half *k*-space high-resolution gradient-recalled EPI *Magn. Reson. Med.* **40** 754–62
[13] Finsterbusch J and Frahm J 2002 Half-Fourier single shot STEAM MRI *Magn. Reson. Med.* **47** 611–5
[14] McGibney G, Smith M R, Nichols S T and Crawley A 1993 Quantitative evaluation of several partial Fourier reconstruction algorithms used in MRI *Magn. Reson. Med.* **30** 51–9
[15] Ahrens E T, Narasimhan P T, Nakada T and Jacobs R E 2002 Small animal neuroimaging using magnetic resonance microscopy *Progr. NMR Spectr.* **440** 175–206
[16] Callaghan P T 1991 *Principles of Nuclear Magnetic Resonance Microscopy* (Oxford: Clarendon)
[17] Ahrens E T and Dubowitz D J 2001 Peripheral somatosensory fMRI in mouse at 11.7 T *NMR Biomed.* **14** 318–24
[18] Roemer P B, Edelstein W A, Hayes C E, Souza S P and Mueller O M 1990 The NMR phased array *Magn. Reson. Med.* **16** 192–225
[19] Frahm J and Hänicke W 1999 Rapid scan techniques *Magnetic Resonance Imaging* 3rd edn, ed D D Stark and W G Bradley (St Louis, MO: Mosby) pp 87–124
[20] Gyngell M L 1989 The steady-state signals in short-repetition-time sequences *J. Magn. Reson.* **81** 474–83
[21] Oppelt A, Graumann R, Barfuss H, Fischer H, Hertl W and Schajor W 1986 FISP: a new fast MRI sequence *Electromedica* **54** 15
[22] Frahm J, Hänicke W and Merboldt K D 1987 Transverse coherence in rapid FLASH NMR imaging *J. Magn. Reson.* **72** 307–14
[23] Haacke E M, Wielopolski P A, Tkach J A and Modic M 1990 Steady-state free precession imaging in the presence of motion: application for improved visualization of the cerebrospinal fluid *Radiology* **175** 545–52
[24] Carr J, Simonetti O, Bundy J, Li D, Pereles S and Finn J P 2001 Cine MR angiography of the heart with segmented true fast imaging with steady-state precession *Radiology* **219** 828–34
[25] Hennig J, Nauerth A, Friedburg H and Ratzel D 1984 Ein neues Schnellbildverfahren für die Kernspintomographie *Radiologe* **24** 579–80
[26] Hennig J, Nauerth A and Friedburg H 1986 RARE imaging: a fast imaging method for clinical MR *Magn. Reson. Med.* **3** 832–3
[27] Carr H Y and Purcell E M 1954 Effects of diffusion on free precession in nuclear magnetic resonance experiments *Phys. Rev.* **94** 630
[28] Meiboom S and Gill D 1958 Modified spin-echo method for measuring nuclear relaxation times *Rev. Sci. Instrum.* **29** 688–91
[29] Hennig J 1988 Multiecho imaging sequences with low refocusing flip angles *J. Magn. Reson.* **78** 397–407
[30] Oshio K and Feinberg D A 1991 GRASE (gradient- and spin-echo) imaging: a novel fast MRI technique *Magn. Reson. Med.* **20** 344–9
[31] Hennig J and Scheffler K 2001 Hyperechoes *Magn. Reson. Med.* **46** 6–12
[32] Mansfield P 1977 Multi-planar image formation using NMR spin echoes *J. Phys. C: Solid State Phys.* **10** L55–8
[33] Mansfield P 1978 Biological and medical imaging by NMR *J. Magn. Reson.* **29** 355–72
[34] Chapman B, Turner R, Ordidge R J, Doyle M, Cawley M, Coxon R, Glover P and Mansfield P 1987 Real-time movie imaging from a single cardiac cycle by NMR *Magn. Reson. Med.* **5** 246–54
[35] Edelman R R, Wielopolski P and Schmitt F 1994 Echo-planar imaging *Radiology* **192** 600–12
[36] Haase A, Frahm J, Hänicke W and Matthaei D 1985 ^{1}H NMR chemical shift selective (CHESS) imaging *Phys. Med. Biol.* **30** 341–4
[37] Stehling M K, Howseman A M, Ordidge R J, Chapman B, Turner R, Coxon R, Glover P, Mansfield P and Coupland R E 1989 Whole-body echo-planar MR imaging at 0.5 T *Radiology* **170** 257–63
[38] Ordidge R J, Howseman A, Coxon R, Turner R, Chapman B, Glover P, Stehling M and Mansfield P 1989 Snapshot imaging at 0.5 T using echo-planar techniques *Magn. Reson. Med.* **10** 227–40
[39] Ahn C B, Kim J H and Cho Z H 1986 High speed spiral-scan echo planar NMR imaging-I *IEEE Trans. Med. Imaging* **5** 2–7
[40] Börnert P, Schomber H, Aldefeld B and Groen J 1999 Improvements in spiral MR imaging *Magn. Reson. Mater. Phys.* **9** 29–41
[41] Block K T 2004 Spiralförmige Abtastung des k-Raumes bei der Magnetresonanz-Tomographie *Diplomarbeit* Georg-August Universität, Göttingen
[42] Sodickson D K and Manning W J 1997 Simultaneous acquisition of spatial harmonics (SMASH): fast imaging with radiofrequency coil arrays *Magn. Reson. Med.* **38** 591–603
[43] Jakob P M, Griswold M A, Edelman R R and Sodickson D K 1998 AUTO-SMASH: a self-calibrating technique for SMASH imaging *Magn. Reson. Mater. Phys.* **7** 42–54
[44] Heidemann R M, Griswold M A, Haase A and Jakob P M 2001 VD-AUTO-SMASH imaging *Magn. Reson. Med.* **45** 1066–74
[45] Griswold M A, Jakob P M, Heidemann R M, Nittka M, Jellus V, Wang J, Kiefer B and Haase A 2002 Generalized autocalibrating partially parallel acquisitions (GRAPPA) *Magn. Reson. Med.* **47** 1202–10
[46] Ra J B and Rim C Y 1993 Fast imaging using subencoding data sets from multiple detectors *Magn. Reson. Med.* **30** 142–5
[47] Pruessmann K P, Weiger M, Scheidegger M B and Boesiger P 1999 SENSE: sensitivity encoding for fast MRI *Magn. Reson. Med.* **42** 952–62
[48] Pruessmann K P, Weiger M, Börnert P and Boesiger P 2001 Advances in sensitivity encoding with arbitrary *k*-space trajectories *Magn. Reson. Med.* **46** 638–51
[49] Bammer R, Keeling S L, Augustin M, Pruessmann K P, Wolf R, Stollberger R, Hartung H P and Fazekas F 2001 Improved diffusion-weighted single-shot echo-planar imaging (EPI) in stroke using sensitivity encoding (SENSE) *Magn. Reson. Med.* **46** 548–54
[50] Jaermann T, Crelier G, Pruessmann K P, Golay X, Netsch T, van Muiswinkel A M C, Mori S, van Zijl P C M, Valavanis A, Kollias S and Boesiger P 2004 SENSE-DTI at 3 T *Magn. Reson. Med.* **51** 230–6
[51] Frahm J, Haase A, Matthaei D, Merboldt K D and Hänicke W 1985 Rapid NMR imaging using stimulated echoes *J. Magn. Reson.* **65** 130–5
[52] Frahm J, Merboldt K D, Hänicke W and Haase A 1985 Stimulated echo imaging *J. Magn. Reson.* **64** 81–93
[53] Finsterbusch J and Koch M A 2003 (Almost) free lunch: single-shot STEAM MRI with GRAPPA *Proc. Intl Soc. Mag. Reson. Med.* **11** 1012
[54] Finsterbusch J and Koch M A 2004 Single-shot STEAM MRI combined with SENSE *Proc. Intl Soc. Mag. Reson. Med.* **12** 2251
[55] Natt O, Watanabe T, Boretius S, Radulovic J, Frahm J and Michaelis T 2002 High-resolution 3D MRI of mouse brain reveals small cerebral structures *in vivo J. Neurosci. Methods* **120** 203–9
[56] Lauterbur P C, Dias M H M and Rudin A M 1978 Augmentation of tissue water proton spin-lattice relaxation

rates by *in vivo* addition of paramagnetic ions *Frontiers of Biological Energetics* vol 1, ed L P Dutton *et al* (New York: Academic) pp 752–9
[57] Runge V M 2000 Safety of approved MR contrast media for intravenous injection *J. Magn. Reson. Imaging* **12** 205–13
[58] Drapeau P and Nachshen D A 1984 Manganese fluxes and manganese-dependent neurotransmitter release in presynaptic nerve endings isolated from rat brain *J. Physiol.* **348** 493–510
[59] Narita K, Kawasaki F and Kita H 1990 Mn and Mg influxes through Ca channels of motor nerve terminals are prevented by verapamil in frogs *Brain Res.* **510** 289–95
[60] Sloot W N and Gramsbergen J B P 1994 Axonal transport of manganese and its relevance to selective neurotoxicity in the rat basal ganglia *Brain Res.* **657** 124–32
[61] Lin Y J and Koretsky A P 1997 Manganese ion enhances in T_1-weighted MRI during brain activation: an approach to direct imaging of brain function *Magn. Reson. Med.* **38** 378–88
[62] Pautler R G, Silvia A C and Koretsky A P 1998 *In vivo* neuronal tract tracing using manganese-enhanced magnetic resonance imaging *Magn. Reson. Med.* **40** 740–8
[63] Watanabe T, Michaelis T and Frahm J 2001 Mapping of retinal projections in the living rat using high-resolution 3D gradient-echo MRI with Mn^{2+}-induced contrast *Magn. Reson. Med.* **46** 424–9
[64] Watanabe T, Radulovic J, Spiess J, Natt O, Boretius S, Frahm J and Michaelis T 2004 In vivo 3D MRI staining of mouse hippocampal system using intracerebral injection of $MnCl_2$ *Neuroimage* **22** 860–7
[65] Watanabe T, Natt O, Boretius S, Frahm J and Michaelis T 2002 *In vivo* 3D MRI staining of mouse brain after subcutaneous application of $MnCl_2$ *Magn. Reson. Med.* **48** 852–9
[66] Dousset V, Delalande C, Ballarino L, Quesson B, Seilhan D, Coussemacq M, Thiaudière E, Brochet B, Canioni P and Caillé J M 1999 *In vivo* macrophage activity imaging in the central nervous system detected by magnetic resonance *Magn. Reson. Med.* **41** 329–33
[67] Hoehn M *et al* 2002 Monitoring of implanted stem cell migration *in vivo*: a highly resolved *in vivo* magnetic resonance imaging investigation of experimental stroke in rat *Proc. Natl Acad. Sci. USA* **99** 16267–72
[68] Frahm J, Merboldt K D, Hänicke W and Haase A 1987 Flow suppression in rapid FLASH NMR images *Magn. Reson. Med.* **4** 372–7
[69] Moran P R 1982 A flow velocity zeugmatographic interlace for NMR imaging in humans *Magn. Reson. Imaging* **1** 197–203
[70] O'Donnell H 1985 NMR blood flow imaging using multiecho, phase contrast sequences *Med. Phys.* **12** 59–64
[71] Masaryk T J, Perl J II, Dagirmanjian A, Tkach J A and Laub G 1999 Magnetic resonance angiography: neuroradiological applications *Magnetic Resonance Imaging* 3rd edn ed D D Stark and W G Bradley (St Louis, MO: Mosby) pp 1277–315
[72] Summers P E, Jarosz J M and Markus H 2001 MR angiography in cerebrovascular disease *Clin. Radiol.* **56** 437–56
[73] Goldstein J P 2003 New techniques and applications for magnetic resonance angiography *Mt Sinai J. Med.* **70** 375–85
[74] Sohn C H, Sevick R J and Frayne R 2003 Contrast-enhanced MR angiography of the intracranial circulation *Magn. Reson. Imaging Clin. N. Am.* **22** 599–614
[75] Moseley M E and Butts K 1999 Diffusion and perfusion *Magnetic Resonance Imaging* 3rd edn, ed D D Stark and W G Bradley (St Louis, MO: Mosby) pp 1515–38
[76] Østergaard L 2004 Cerebral perfusion imaging using bolus tracking *Top. Magn. Reson. Imaging* **15** 3–9
[77] Haase A, Matthaei D, Hänicke W and Frahm J 1986 Dynamic digital subtraction imaging using fast low-angle shot movie sequences *Radiology* **160** 537–41
[78] Detre J A, Leigh J S, Williams D S and Koretsky A P 1992 Perfusion imaging *Magn. Reson. Med.* **23** 37–45
[79] Stejskal E O 1965 Use of spin echos in a pulsed magnetic-field gradient to study anisotropic, restricted diffusion and flow *J. Chem. Phys.* **43** 3597–603
[80] Stejskal E O and Tanner J E 1965 Spin diffusion measurements: spin echoes in the presence of a time-dependent field gradient *J. Chem. Phys.* **42** 288–92
[81] Nolte U, Finsterbusch J and Frahm J 2000 Rapid isotropic diffusion mapping without susceptibility artefacts: whole brain studies using diffusion-weighted single-shot STEAM MR imaging *Magn. Reson. Med.* **44** 731–6
[82] Lövbald K O, Baird A E, Schlauch G, Benfield A, Siewert B, Voetsch B, Connor A, Burzynski C, Edelman R R and Warach S 1997 Ischemic lesion volumes in acute stroke by diffusion-weighted magnetic resonance imaging correlate with clinical outcome *Ann. Neurol.* **42** 164–70
[83] Lutsep H L, Albers G W, DeCrespigny A, Kamat G, Marks M P and Moseley M 1997 Clinical utility of diffusion-weighted magnetic resonance imaging in the assessment of ischemic stroke *Ann. Neurol.* **41** 574–80
[84] Gore J C and Kennan R P 1999 Physical and physiological basis of magnetic relaxation *Magnetic Resonance Imaging* 3rd edn ed D D Stark and W G Bradley (St Louis, MO: Mosby) pp 33–42
[85] Ulmer J L, Mathews V P, Hamilton C A and Elster A D 1999 Magnetization transfer imaging of the brain *Magnetic Resonance Imaging* 3rd edn, ed D D Stark and W G Bradley (St Louis, MO: Mosby) pp 1539–53
[86] Le Bihan D 1995 Molecular diffusion, tissue microdynamics and microstructure *NMR Biomed.* **8** 375–86
[87] Moseley M E, Cohen Y, Kucharczyk J, Mintorovitch J, Asgari H S, Wendland M F, Tsuruda J and Norman D 1990 Diffusion-weighted MR imaging of anisotropic water diffusion in cat central nervous system *Radiology* **176** 439–45
[88] Chenevert T L, Brunberg J A and Pipe J 1990 Anisotropic diffusion in human white matter: demonstration with MR techniques *in vivo Radiology* **177** 401–5
[89] Basser P J and Pierpaoli C 1996 Microstructural and physiological features of tissues elucidated by quantitative diffusion-tensor MRI *J. Magn. Reson.* B **111** 209–19
[90] Mori S, Crain B J, Chacko V P and van Zijl P C 1999 Three-dimensional tracking of axonal projections in the brain by magnetic resonance imaging *Ann. Neurol.* **45** 265–9
[91] Basser P J, Pajevic S, Pierpaoli C, Duda J and Aldroubi A 2000 *In vivo* fiber tractography using DT-MRI data *Magn. Reson. Med.* **44** 625–32
[92] Torrey H C 1953 Nuclear spin relaxation by translational diffusion *Phys. Rev.* **92** 962–9
[93] Basser P J, Mattiello J and Le Bihan D 1994 Estimation of effective self-diffusion tensor from the NMR spin echo *J. Magn. Reson.* **103** 247–54
[94] Le Bihan D, Mangin J, Poupon C, Clark C A, Pappata S, Molko N and Chabriat H 2001 Diffusion tensor imaging: concepts and applications *J. Magn. Reson. Imaging* **13** 534–46
[95] Frahm J, Dechent P, Baudewig J and Merboldt K D 2004 Advances in functional MRI of the human brain *Progr. NMR Spectr.* **44** 1–32
[96] Zhan W, Gu H, Xu S, Silbersweig D A, Stern E and Yang Y 2003 Circular spectrum mapping for intravoxel fiber structures based on high angular resolution apparent diffusion coefficients *Magn. Reson. Med.* **49** 1077–88
[97] Assaf Y, Ben-Bashat D, Chapman J, Peled S, Biton I E, Kafri M, Segev Y, Hendler T, Korczyn A D, Graif M and Cohen Y 2002 High *b*-value *q*-space analyzed diffusion-weighted MRI: application to multiple sclerosis *Magn. Reson. Med.* **47** 115–26

[98] Ogawa S, Lee T M, Kay A R and Tank D W 1990 Brain magnetic resonance imaging with contrast depending on blood oxygenation *Proc. Natl Acad. Sci. USA* **87** 9868–72
[99] Kwong K K *et al* 1992 Dynamic magnetic resonance imaging of human brain activity during primary sensory stimulation *Proc. Natl Acad. Sci. USA* **89** 5675–9
[100] Bandettini P A, Wong E C, Hinks R S, Tikofsky R S and Hyde J S 1992 Time course EPI of human brain function during task activation *Magn. Reson. Med.* **25** 390–7
[101] Frahm J, Bruhn H, Merboldt K D and Hänicke W 1992 Dynamic MRI of human brain oxygenation during rest and photic stimulation *J. Magn. Reson. Imaging* **2** 501–5
[102] Blamire A M, Ogawa S, Ugurbil K, Rothman D, McCarthy G, Ellermann J M, Hyder F, Rattner Z and Shulman R G 1992 Dynamic mapping of the human visual cortex by high-speed magnetic resonance imaging *Proc. Natl Acad. Sci. USA* **89** 11069–73
[103] Baudewig J, Dechent P, Merboldt K D and Frahm J 2003 Thresholding in correlation analyses of magnetic resonance functional neuroimaging *Magn. Reson. Imaging* **21** 1121–30
[104] Dechent P and Frahm J 2000 Direct mapping of ocular dominance columns in human primary visual cortex *Neuroreport* **11** 3247–9
[105] Menon R S and Goodyear B G 1999 Submillimeter functional localization in human striate cortex using BOLD contrast at 4 Tesla: implications for the vascular point-spread function *Magn. Reson. Med.* **41** 230–5
[106] Cheng K, Waggoner R and Tanaka K 2001 Human ocular dominance columns as revealed by high-field functional magnetic resonance imaging *Neuron* **32** 359–74
[107] Goodyear B and Menon R 2001 Brief visual stimulation allows mapping of ocular dominance in visual cortex using fMRI *Hum. Brain Mapp.* **14** 210–7
[108] Horton J C and Hedley-Whyte E T 1984 Mapping of cytochrome oxidase patches and ocular dominance colums in human visual cortex *Phil. Trans. R. Soc. Lond.* B **304** 255–72